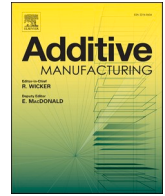




Contents lists available at ScienceDirect

Additive Manufacturing

journal homepage: www.elsevier.com/locate/addma

Design and validation of 3D self-supporting structures and printing paths for multi-axis additive manufacturing

Qichen Guo^a, Jun Ye^{b,*}, Hongjia Lu^{c,*}, Guan Quan^a, Zhen Wang^d, Yang Zhao^a, Yi Min Xie^c

^a College of Civil Engineering and Architecture, Zhejiang University, Hangzhou 310058, China

^b School of Civil Engineering, University of Leeds, Leeds LS2 9JT, UK

^c Centre for Innovative Structures and Materials, School of Engineering, RMIT University, Melbourne 3001, Australia

^d Department of Civil Engineering, Hangzhou City University, Hangzhou 310015, China

ARTICLE INFO

Key words:

Topology optimisation
Overhang constraint
Multi-axis AM
Self-supporting structure

ABSTRACT

Additive manufacturing (AM) has become a widely used tool for fabricating components with complex geometries. However, the overhang effect induced by gravity often necessitates additional supports to prevent collapse and warping during the printing process. To address this issue, previous studies incorporated overhang constraints to the topology optimisation to create self-supporting structures. Nevertheless, these studies primarily focused on 3-axis AM, which deposits material in a single direction and often compromises structural stiffness to achieve self-supporting designs. In response, this study aims to design 3D self-supporting structures tailored for multi-axis AM. By leveraging the rotatable base platform of multi-axis systems, this approach automatically identifies optimised local build directions and the corresponding structural topology to minimise overhangs. The effectiveness of this approach is demonstrated through several numerical examples, with results validated numerically via printing simulations in VERICUT and physically using a multi-axis Wire Arc Additive Manufacturing (WAAM) machine. The results indicate that the performance degradation caused by 3-axis-based overhang constraints can be reduced to a negligible level with the multi-axis-based approach.

1. Introduction

Topology optimisation (TO) has been widely employed to identify structures with prominent performance, such as maximised stiffness or minimised material consumption [1–4]. It leverages advanced mathematical algorithms to systematically explore the design space and identify an efficient material distribution within a given design domain. However, the complex geometries and intricate internal features resulting from TO are often challenging to produce using traditional manufacturing techniques. To address the problem, additive manufacturing (AM), also known as 3D printing, has frequently been utilised [5–7]. Unlike traditional manufacturing methods, AM constructs components by precisely depositing material layer by layer, enabling the creation of complex geometries with high fidelity and structural integrity [8]. Over the past decade, the application of metal AM in the construction industry has attracted significant interest. The technology has evolved from producing small-scale nodal components [9–11] (Fig. 1(a)) to larger structural elements such as beams and columns [12,13] (Fig. 1(b)), and even entire structures like pedestrian

bridges [14,15] (Fig. 1(c)). A notable example is the MX3D bridge in Amsterdam [15] (Fig. 1(c)), which stands as the world's first 3D-printed steel bridge and showcases the potential of metal AM for large-scale construction projects. Additionally, metal AM has been utilised in creating custom façade elements, intricate architectural features, and specialised structural connectors that are challenging to produce using conventional methods. The integration of AM with advanced design optimisation tools further enhances its applicability, allowing for more efficient material usage and reduced waste.

However, the current AM technique still does not guarantee the full printability of structures with arbitrary geometry. Consequently, the design freedom of TO remains limited by a range of manufacturing constraints, such as element size [16], machining [17] and connectivity constraints [18]. Several studies focused on addressing these challenges. For example, Lianos et al. [19] focused on designing manufacturable structures using the Direct Energy Deposition (DED) technique. Gu et al. [20] introduced an approach that allows flexible selection between two types of supports within the same enclosed void. Bikas et al. [21] adopted topology optimisation to reduce the volume of additive

* Corresponding authors.

E-mail addresses: J.Ye2@leeds.ac.uk (J. Ye), hongjia.lu@rmit.edu.au (H. Lu).

<https://doi.org/10.1016/j.addma.2024.104563>

Received 8 July 2024; Received in revised form 31 October 2024; Accepted 16 November 2024

Available online 19 November 2024

2214-8604/© 2024 The Author(s). Published by Elsevier B.V. This is an open access article under the CC BY-NC-ND license (<http://creativecommons.org/licenses/by-nc-nd/4.0/>).

manufacturing components, thereby decreasing printing time. Stavropoulos et al. [22] adopted a hybrid strategy combining additive and subtractive manufacturing to enhance manufacturability. Among the AM-related challenges, one critical challenge is the overhang effect [23–26], which refers to the wrapping or collapsing of printed components due to gravity. Specifically, as shown in Fig. 2, when the overhang angle of the component's boundary θ_{ov} (i.e., the angle between the component boundary and vertical direction) exceeds a threshold θ_{max} , the deposited material fails to fully consolidate, degrading the quality of the print. To address this, support structures are often added beneath overhanging boundaries [27,28], though this solution increases material use and impacts the surface quality upon removal. Therefore, the design of self-supporting structures, which satisfy the overhang constraints without additional support, has garnered significant research interest. Innovative approaches include Stavropoulos et al.'s software [29], which assesses the manufacturability of AM components and offers design modifications to enhance printability; Leary et al.'s post-processing approach for efficient, support-free structures [30]; Gaynor et al.'s integration of overhang constraints through layer-wise projection in TO [31]; and Langelaar et al.'s simultaneous optimisation of both structural topology and supports with consideration of build direction [32]. Furthermore, Pellens et al. [33] addressed the overhang problem by utilising four different elemental filters to eliminate elements violating overhang and minimum size constraints. Zhang et al. [34] applied overhang constraints by restricting the member orientation using Heaviside projection functions. Garaigordobil et al. [35] leveraged the SUSAN contour detection algorithm to define structural boundaries, allowing explicit overhang constraints to be included in the optimisation process. Wang et al. generated the self-supporting lattice structures within the topology optimisation framework [36]. Jiang et al. designed a sequential strategy integrated with the constraints of overhang and connectivity [37]. Despite the extensive research on self-supporting structures, most research has been limited to 3-axis AM. Findings from these studies reveal that when dealing with problems with low volume fractions (i.e., the ratio between the structure and the design domain), the compromises in structural stiffness are often substantial [38].

In recent years, a novel AM technique, multi-axis AM, has emerged as a promising approach to address the overhang problem [39,40]. Unlike traditional 3-axis machines, multi-axis machines feature a rotatable platform, enabling dynamically adjustable build directions [41]. This flexibility allows for the customisation of build directions to minimise the overhang effect. However, careful consideration is required to avoid collisions between the printed component and the printing nozzle. Leveraging the capabilities of multi-axis AM, some studies have sought to reduce the overhang effect by decomposing structures into several parts and assigning distinct local build directions to each [42,43]. In addition, other studies have explored the customisation of curved printing surfaces to avoid the overhang effect [44–47]. Despite these

advancements, existing studies mainly focus on the optimisation of the printing path, which does not guarantee fully support-free printing in all cases. Significantly, the integrated optimisation of both the printing strategy and structural topology remains largely unexplored.

To fully exploit the flexibility of multi-axis AM, an approach that optimises both the structural topology and multi-axis printing surfaces was proposed in [48]. Although it can greatly reduce the sacrifices of structural performance caused by overhang constraints, it is limited to 2D problems. In this study, we extend the previous approach to 3D cases. To manage the complexity of overhang constraints in 3D, the local build directions are projected onto two orthogonal planes, simplifying the numerical computations. Additionally, to minimise collision risks during multi-axis printing, a turning angle constraint is applied to control the overall concavity of the printing surface. The optimised results are then validated numerically and physically to demonstrate the effectiveness of the proposed approach. The rest of the paper is organised as follows: Section 2 briefly reviews previous related studies; Section 3 details the 3D multi-axis optimisation approach; Section 4 provides several numerical examples to demonstrate the effectiveness of the proposed approach; results are validated using numerical simulations and physical printing in Section 5. Finally, conclusions are summarised in Section 6.

2. Preliminary knowledge

The new approach for 3D structures builds upon the previously established 2D approach [48]. Therefore, we briefly review this approach in this section. As illustrated in Fig. 3(a), the design process starts with an optimised solution from the traditional topology optimisation utilising the Solid Isotropic Material with Penalisation scheme (SIMP), and involves two main steps. In the first step, the design domain is subdivided into printing zones, each accommodating a single local build direction that corresponds to a series of inclined and flat printing surfaces. A linear optimisation problem is then solved to determine the optimal build directions that maximise the structure's printable proportion (i.e., Fig. 3(b)). If the proportion of printable boundary elements r_{unp} falls below the predefined satisfactory threshold of 1 % (i.e., a numerical tolerance), a second re-optimisation step is performed to redesign the structure and eliminate any remaining unprintable elements (see Fig. 3(c)). Once resolved, the multi-axis printing path is established by guiding the print nozzle along the optimised printing surfaces (i.e., Fig. 3(d)). For completeness, details of the two optimisation steps are reviewed in the following Sections 2.1 and 2.2.

2.1. Printing plan optimisation for a given structure

In the printing plan optimisation, the structure is treated as given constant and the following optimisation problem is solved to obtain the

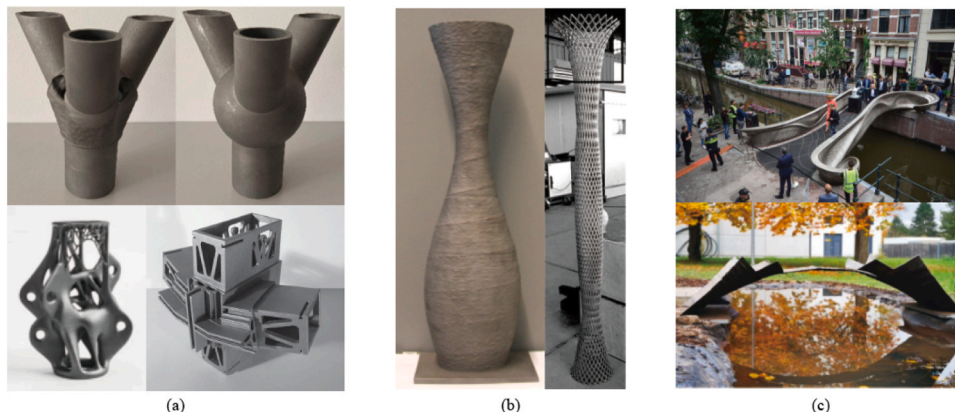


Fig. 1. Metal printed structures: (a) joint structures [9–11]; (b) column structures [12,13]; (c) pedestrian bridges [14,15].

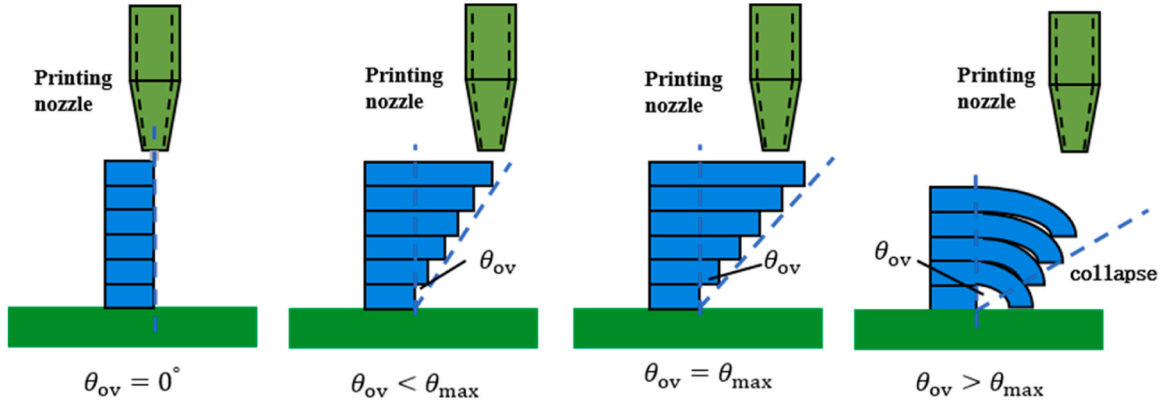


Fig. 2. Effects of different overhang angle θ_{ov} : (a) $\theta_{ov} = 0^\circ$; (b) $\theta_{ov} < \theta_{max}$ and (c) $\theta_{ov} = \theta_{max}$; (d) $\theta_{ov} > \theta_{max}$, where θ_{max} denotes the maximum overhang angle.

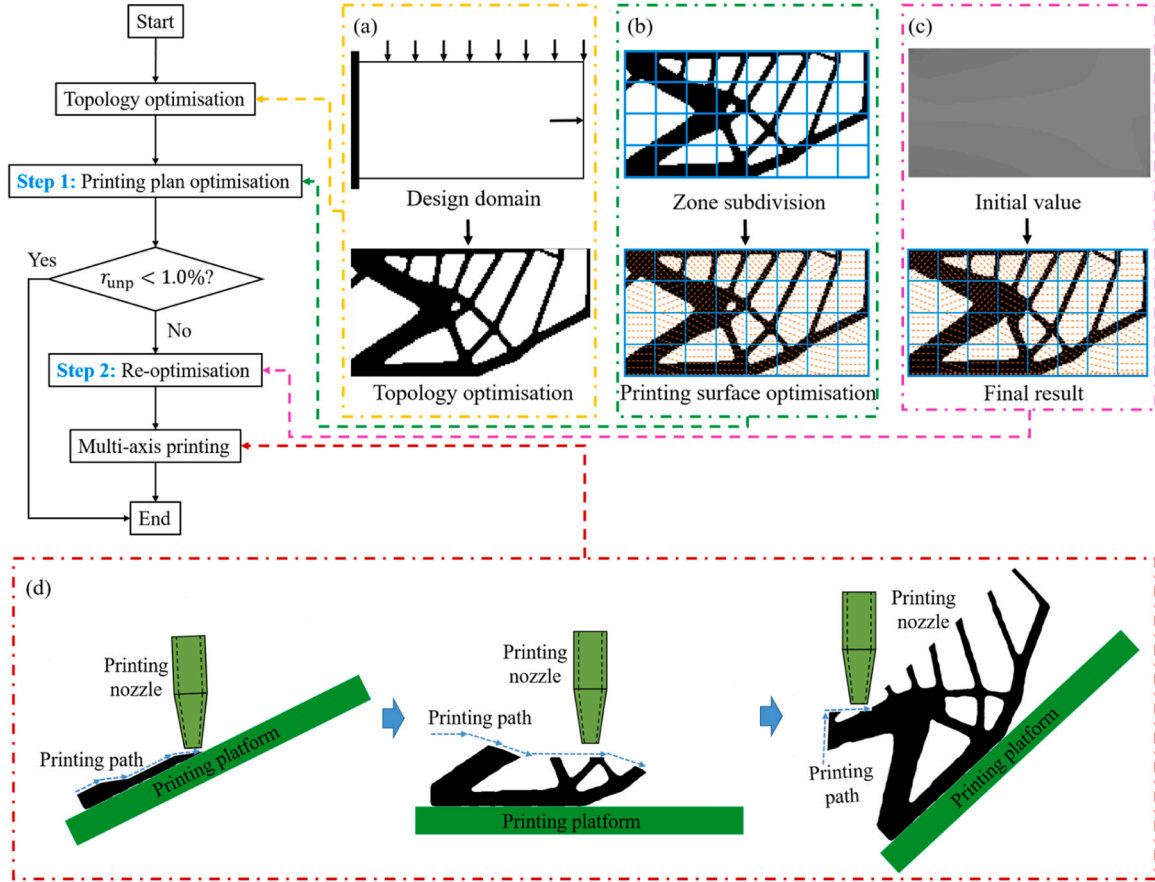


Fig. 3. Workflow of the 2D optimisation approach for multi-axis AM: (a) optimised solution from the traditional topology optimisation is used as the starting point; (b) identify optimal printing surfaces for given structure, where dashed lines in each zone represent the local printing paths; (c) re-optimize the structure to reduce overhang; (d) printing process using the identified printing paths; r_{unp} represents the ratio of unprintable boundary elements and 1 % is a numerical tolerance for the total printability.

build directions that maximise the structure's printable proportion:

$$\text{find : } \boldsymbol{\theta} = [\theta_1, \theta_2, \dots, \theta_{n_z}]^T \quad (1a)$$

$$\text{min : } P = \mathbf{O}^T \boldsymbol{\eta} \quad (1b)$$

$$\text{s.t. : } \mathbf{O} = |\mathbf{M}\boldsymbol{\theta} - \boldsymbol{\varphi} - \theta_{max}| + |\mathbf{M}\boldsymbol{\theta} - \boldsymbol{\varphi} + \theta_{max}| - 2\theta_{max} \quad (1c)$$

$$\boldsymbol{\theta}_{next} - \boldsymbol{\theta}_{first} < \boldsymbol{\theta}_{t,max}, \quad (1d)$$

where $\boldsymbol{\theta} = [\theta_1, \theta_2, \dots, \theta_{n_{ele}}]^T$ represents the local build direction vector,

with n_{ele} denoting the number of elements; $\mathbf{O} = [O_1, O_2, \dots, O_i, \dots, O_{n_{ele}}]^T$ is the element overhang violation vector, with O_i being continuous and indicating the overhang violation of the i th element. Specifically, $O = 0$ denotes a printable element, while $O > 0$ denotes an unprintable element. The value of P is also continuous and represents the total overhang violation across all boundary elements. It is important to note that r_{unp} and P have different meanings, as the values of O can vary among unprintable elements. Only when the structure is fully printable do both r_{unp} and P equal zero. $\boldsymbol{\eta} = [\eta_1, \dots, \eta_i, \dots, \eta_{n_{ele}}]^T$, with $\eta_i \in \{0, 1\}$ denoting the weighting factor for the i th element. \mathbf{M} is a 0–1 mapping

matrix used to determine the corresponding zone for each element; $\varphi = [\varphi_1, \varphi_2, \dots, \varphi_{n_{ele}}]^T$ is the elemental orientation angle vector; θ_{max} is the maximum overhang angle; θ_{next} and θ_{first} are the build direction vectors of adjacent zones; $\theta_{t,max}$ is the maximum turning angle. Equations (1) demonstrates a linear programming problem. It can be efficiently solved using interior point solvers, such as MOSEK [54], with the optimised solutions guaranteed to be the global optimum.

2.2. Re-optimisation

Since the structure is treated as constant in the first step, the optimised printing surfaces cannot ensure full printability. If the proportion of unprintable elements is not satisfactory, i.e., exceeds 1 %, a second re-optimisation step is initiated. It's important to note that this 1 % threshold is a numerical allowance to account for the occasional presence of a small number of unprintable voxel elements in the optimised solution, which do not impact the overall printability of the model. In this re-optimisation step, the printing surfaces identified in step 1 are used as inputs to redesign the structure, aiming to eliminate any remaining overhanging elements. Specifically, the following topology optimisation problem is solved:

$$\text{find : } \rho = [\rho_1, \rho_2, \dots, \rho_{n_{ele}}]^T \quad (2a)$$

$$\text{min : } C(\rho) = \mathbf{F}^T \mathbf{U} = \mathbf{U}^T \mathbf{K}(\rho) \mathbf{U}, \quad (2b)$$

$$\text{s.t. : } \mathbf{K}(\rho) \mathbf{U} = \mathbf{F}, \quad (2c)$$

$$\frac{\sum_{i=1}^{n_{ele}} v_i \rho_i}{\sum_{i=1}^{n_{ele}} v_i} \leq f, \quad (2d)$$

$$\frac{\sum_{i=1}^{n_{ele}} \omega_i(\theta_j) v_i \rho_i}{\sum_{i=1}^{n_{ele}} v_i} \leq 0, \quad (2e)$$

$$0 \leq \rho_i \leq 1, \quad \text{with } i = 1, 2, \dots, n_{ele}, \quad (2f)$$

where $\omega_i(\theta_j)$ evaluates the printability of the i th element under its corresponding build direction θ_j , with the subscript j denoting the zone index. Further details about this optimisation problem can be found in [48].

3. Optimising 3D structures for multi-axis AM

In this section, we extend the 2D multi-axis optimisation approach to 3D applications. The workflow for the 3D approach adheres to the same process as the 2D approach shown in Fig. 3. However, adjustments are necessary to accommodate geometric attributes in 3D problems, such as the representation of local build directions and the calculation of density gradients. These modifications will be described in detail in the subsequent subsections 3.1 and 3.2.

3.1. 3D printing plan optimisation

3.1.1. Zone subdivisions and local build directions

For the design of local build directions, first, we introduce the domain subdivision approach. For simplicity, here the design domain is subdivided by employing a rectangular grid with uniform spacing, as shown in Fig. 4. Note that the zone arrangement that can lead to a fully printable structure is not unique; in general, smaller zones yield more ideal solutions with higher printable proportions. However, excessively small zone sizes are impractical due to high computational demands. More critically, very small zones can cause rapid changes in build directions, which are unfeasible in actual printing processes. The influence of different zone sizes is discussed in detail in Section 4.5.

The representation of local build direction in each zone is depicted in Fig. 5. In 2D cases, the local build direction is represented by its intersection angle with the positive x-axis (Fig. 5(a)). When extended to 3D cases, we use two angles θ_x and θ_y , which denote the projected angles of θ on xoz and $yozy$ planes, respectively (Fig. 5(b)).

3.1.2. Elemental density gradient

With the printing zones and local build direction defined, next we introduce the evaluation of the elemental density gradient $\nabla \rho$, which is used to determine the local boundary orientation vector γ , as illustrated in Fig. 6. In our proposed approach, printability is assessed exclusively for boundary elements, since all internal elements are inherently supported by the boundary or adjacent internal elements. A boundary element is considered printable if the intersection angle between its associated boundary orientation vector γ and the local build direction is less than the maximum overhang angle θ_{max} . In the 2D context, as shown in Fig. 6(a), the density gradient of an element is evaluated using the densities of the surrounding eight elements. When extended to 3D scenarios, for a given element i , the density gradient direction $\nabla \rho_i$ is calculated using the densities of its 26 neighbouring elements, from ρ_1^i to ρ_{26}^i , see Fig. 6(b):

$$\nabla \rho_i = [a_i, b_i, c_i]^T, \quad (3)$$

where a_i , b_i and c_i can be obtained from:

$$a_i = \frac{1}{18} \sum_{j \in N_1} \rho_j^i - \frac{1}{18} \sum_{j \in N_2} \rho_j^i, \quad (4a)$$

$$N_1 = \{1, 2, 3, 4, 5, 6, 7, 8, 9\}, N_2 = \{18, 19, 20, 21, 22, 23, 24, 25, 26\},$$

$$b_i = \frac{1}{18} \sum_{j \in N_3} \rho_j^i - \frac{1}{18} \sum_{j \in N_4} \rho_j^i, \quad (4b)$$

$$N_3 = \{3, 12, 20, 6, 14, 23, 9, 17, 26\}, N_4 = \{1, 10, 18, 4, 13, 21, 7, 15, 24\},$$

$$c_i = \frac{1}{18} \sum_{j \in N_5} \rho_j^i - \frac{1}{18} \sum_{j \in N_6} \rho_j^i, \quad (4c)$$

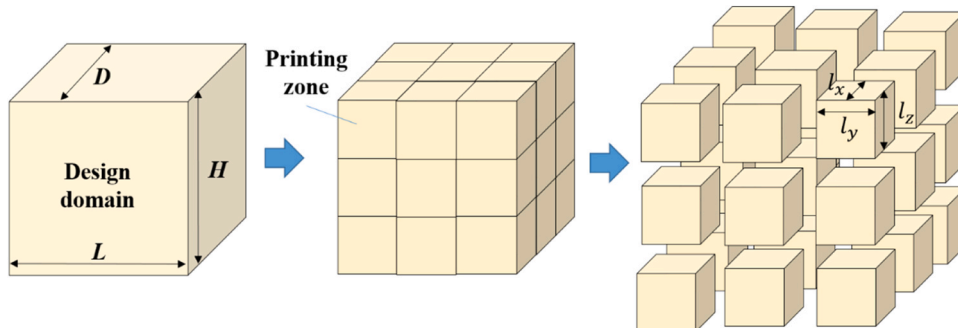


Fig. 4. Regular grid subdivision approach.

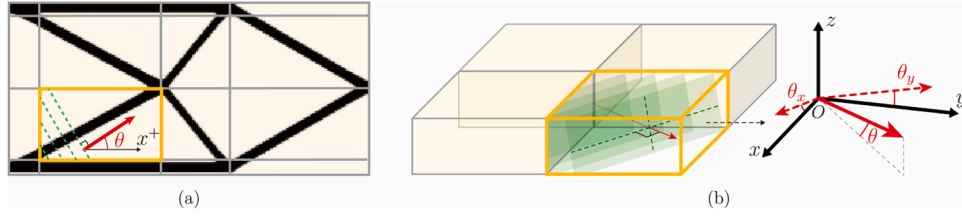


Fig. 5. Printing zones, printing surfaces (i.e., green lines and surfaces) and local build directions (i.e., red arrows): (a) in 2D problems, the build direction is represented by its intersection angle θ with the positive x-axis; (b) in 3D problem, the build direction is represented by θ_x and θ_y in the xoz and $yozy$ planes, respectively.

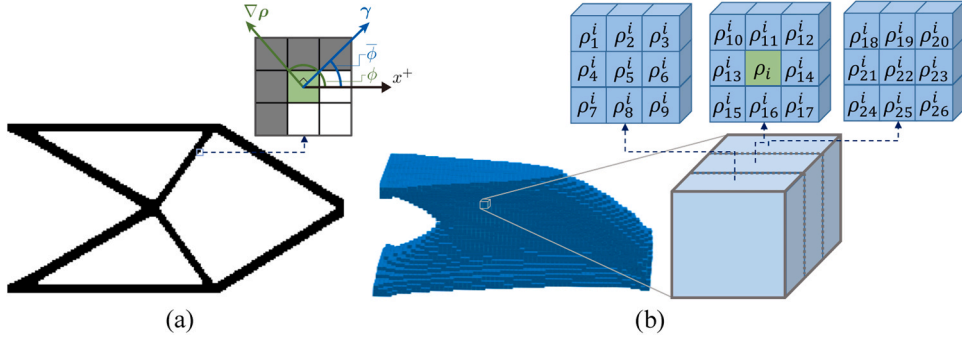


Fig. 6. Elemental density gradient: (a) in 2D problems, the density gradient $\nabla\rho$ is calculated using the densities of the surrounding eight elements and is represented by angle ϕ ; the boundary orientation vector γ is orthogonal to the density gradient, and is represented by angle $\bar{\phi}$; (b) in 3D problems, the density gradient $\nabla\rho$ is calculated based on the densities of the surrounding 26 elements.

$N_5 = \{1, 2, 3, 10, 11, 12, 18, 19, 20\}$, $N_6 = \{7, 8, 9, 15, 16, 17, 24, 25, 26\}$.

Same as the build direction in Fig. 5, we represent the density gradient using the projected angles ϕ_x and ϕ_y in xoz and $yozy$ planes, respectively:

$$\phi_{ix} = \cos^{-1}(a_i / \sqrt{a_i^2 + c_i^2}) \quad (5a)$$

$$\phi_{iy} = \cos^{-1}(b_i / \sqrt{b_i^2 + c_i^2}) \quad (5b)$$

Considering that the structural components are typically built from the bottom up, the following relation can be utilised to determine the structural boundary orientation angle $\bar{\phi}_{ix}$, which is orthogonal to the density gradient direction (Fig. 6(a)):

$$\bar{\phi}_{ix} = \begin{cases} \phi_{ix} + \frac{\pi}{2}, & \text{if } 0 \leq \phi_{ix} \leq \frac{\pi}{2} \\ \phi_{ix} - \frac{\pi}{2}, & \text{if } \frac{\pi}{2} \leq \phi_{ix} \leq \frac{3}{2}\pi \\ \phi_{ix} - \frac{3}{2}\pi, & \text{if } \frac{3}{2}\pi \leq \phi_{ix} \leq 2\pi \end{cases}, \quad (6)$$

Note that the relation demonstrated in Eq. (6) also applies to ϕ_{iy} and $\bar{\phi}_{iy}$.

3.1.3. Optimise local build direction

For an element to be self-supportable, its associated boundary orientation vector must be closely aligned with the build direction. To ensure this alignment, we employ the following two constraints to restrict the build direction on the two projection planes:

$$|\theta_{jx} - \bar{\phi}_{ix} - \theta_{\max}| + |\theta_{jx} - \bar{\phi}_{ix} + \theta_{\max}| = 2\theta_{\max}, \quad (7a)$$

$$|\theta_{jy} - \bar{\phi}_{iy} - \theta_{\max}| + |\theta_{jy} - \bar{\phi}_{iy} + \theta_{\max}| = 2\theta_{\max}, \quad (7b)$$

Note that Eqs. (7a) and (7b) represent a less conservative constraint,

which may allow the intersection angle between the boundary orientation vector and the build direction to exceed θ_{\max} . However, these equations are linear functions, which significantly reduce computational costs. Additionally, any potential overhang violations can be further addressed during the re-optimisation step.

Equations (7) correspond to the printability of a single element. To maximise the printable proportion of the entire structure, the following optimisation problem can be solved:

$$\text{find : } \theta_x = [\theta_{1,x}, \theta_{2,x}, \dots, \theta_{n_x,x}] \text{ and } \theta_y = [\theta_{1,y}, \theta_{2,y}, \dots, \theta_{n_y,y}] \quad (8a)$$

$$\text{min : } P = \mathbf{O}_x^T \boldsymbol{\eta} + \mathbf{O}_y^T \boldsymbol{\eta} \quad (8b)$$

$$\text{s.t. : } \mathbf{O}_x \geq |\mathbf{M}\theta_x - \bar{\boldsymbol{\phi}}_x - \theta_{\max}| + |\mathbf{M}\theta_x - \bar{\boldsymbol{\phi}}_x + \theta_{\max}| - 2\theta_{\max} \quad (8c)$$

$$\mathbf{O}_y \geq |\mathbf{M}\theta_y - \bar{\boldsymbol{\phi}}_y - \theta_{\max}| + |\mathbf{M}\theta_y - \bar{\boldsymbol{\phi}}_y + \theta_{\max}| - 2\theta_{\max}, \quad (8d)$$

where P is the total overhang violation of the optimised structure; $\mathbf{O}_x = [O_{1,x}, O_{2,x}, \dots, O_{n_{ele},x}]^T$ and $\mathbf{O}_y = [O_{1,y}, O_{2,y}, \dots, O_{n_{ele},y}]^T$ represent vectors of element overhang violations in xoz and $yozy$ planes, respectively; $\boldsymbol{\eta} = [\eta_1, \dots, \eta_i, \dots, \eta_{n_{ele}}]^T$, with $\eta_i = 1$ for the boundary elements and $\eta_i = 0$ for all other elements; \mathbf{M} is a 0–1 mapping matrix used to obtain the corresponding zone of each element; $\theta_x = [\theta_{1,x}, \theta_{2,x}, \dots, \theta_{n_x,x}]^T$ and $\theta_y = [\theta_{1,y}, \theta_{2,y}, \dots, \theta_{n_y,y}]^T$ are the local build direction vectors in xoz and $yozy$ planes, respectively, with n_x denoting the number of zones; $\bar{\boldsymbol{\phi}}_x = [\bar{\phi}_{1,x}, \bar{\phi}_{2,x}, \dots, \bar{\phi}_{n_{ele},x}]^T$ and $\bar{\boldsymbol{\phi}}_y = [\bar{\phi}_{1,y}, \bar{\phi}_{2,y}, \dots, \bar{\phi}_{n_{ele},y}]^T$ are the elemental orientation angle vectors in xoz and $yozy$ planes, respectively. In addition, to enhance numerical robustness, two types of definitively printable elements, those directly attached to the base platform and those printable across all base platform orientations, can be excluded from the objective function. This exclusion is achieved by setting their η values to zero. Detailed information on this process can be found in [48].

Since the objective function and the constraints are linear, the optimisation problem expressed by Equations (8) demonstrates a linear programming problem which can be efficiently solved using MOSEK [54], with the optimised solutions guaranteed to be the global optimum.

3.2. Collision constraint

Multi-axis printing offers more flexibility than traditional 3D printing; however, it also introduces a risk of collision between the print nozzle and the already printed components. In our approach, we assume that each layer is always deposited directly on top of the preceding layer. Therefore, if the nozzle does not collide with the preceding layer, it cannot collide with material deposited in earlier layers, as this would require penetrating the preceding layer first. Based on this assumption, the collision risk between the nozzle and preceding layer varies based on the shape of the printing surfaces. As shown in Fig. 7(a) to (c), there is no collision risk with convex surfaces, a low risk with slightly concave surfaces (i.e., with a small turning angle), and a high risk with deeply concave surfaces (i.e., with a large turning angle). Therefore, we introduce constraints on turning angles into the printing plan optimisation problem (i.e., Eq. (9)) to control the collision risk. In 2D cases, the turning angle θ_t refers to the change between the local build directions of two adjacent zones, as shown in Fig. 7(d). It can be expressed by:

$$\theta_t = \theta_{\text{next}} - \theta_{\text{first}} \quad (9)$$

In 3D cases, we restrict the turning angles on the xoz and $yozy$ planes, as shown in Fig. 7(e):

$$\theta_{t,x} = \theta_{\text{next},x} - \theta_{\text{first},x} \leq \theta_{t,\text{max}}, \quad (10a)$$

$$\theta_{t,y} = \theta_{\text{next},y} - \theta_{\text{first},y} \leq \theta_{t,\text{max}}, \quad (10b)$$

where $\theta_{\text{first},x}$ and $\theta_{\text{next},x}$ refer to projected build directions of two adjacent zones in the xoz plane; $\theta_{\text{first},y}$ and $\theta_{\text{next},y}$ are build directions of two adjacent zones in the $yozy$ plane; $\theta_{t,\text{max}}$ denotes a prescribed maximum turning angle. It is worth noting that although the turning angle constraints are applied locally between adjacent zones, the primary goal is to use these local constraints to collectively control the concavity of the global printing surface, thereby reducing collision risk. In addition, $\theta_{t,\text{max}}$ relates to the flexibility and size of the printing nozzle. For printing nozzles with a relatively sharp shape, the risk of collision is reduced, allowing for a relatively high $\theta_{t,\text{max}}$. Conversely, a blunt-shaped nozzle necessitates a lower $\theta_{t,\text{max}}$. When $\theta_{t,\text{max}} = 0$, the printing surface can only be horizontal or convex, ensuring a collision-free printing process for printing nozzles with arbitrary shape [49].

In addition, the zone printing surfaces can be discontinuous as shown in Fig. 8(a), de-validating the turning angle constraints on controlling

the collision risk. Therefore, we employ the following constraints to preserve the continuity of printing surfaces, as shown in Fig. 8(b):

$$\forall \eta, \zeta \in \mathcal{P}, \theta_{\eta,x} = \theta_{\zeta,x}, \quad (11a)$$

$$\forall \eta, \zeta \in \mathcal{C}, \theta_{\eta,y} = \theta_{\zeta,y}, \quad (11b)$$

where \mathcal{P} represents a set including zones in the same row, and \mathcal{C} represents a set including zones in the same column. For the four-zone example shown in Fig. 8, the following relationships hold: $\theta_{1,x} = \theta_{2,x}$; $\theta_{3,x} = \theta_{4,x}$; $\theta_{1,y} = \theta_{3,y}$; and $\theta_{2,y} = \theta_{4,y}$.

Equations (10) and (11) can be integrated into the printing plan optimisation problem, as outlined in Equations (8), to control the turning angles of the printing surfaces and manage collision risks. Since these additional equations are all linear, they do not compromise the convexity of the optimisation problem.

3.3. Re-optimisation

Although the printing plan optimisation identifies optimal printing surfaces, it cannot guarantee complete printability, as the structure is assumed to be constant. Consequently, if the printing surfaces do not achieve a satisfactory printable proportion, a re-optimisation of the structure is necessary to eliminate overhang elements. In this phase, the local build directions determined during the printing plan optimisation are held constant, preserving the overall structural layout and minimising performance degradation. By incorporating the multi-axis overhang constraint (i.e. Constraint (2e)) into the traditional topology optimisation problem, we define the re-optimisation formulation as follows:

$$\text{find : } \boldsymbol{\rho} = [\rho_1, \rho_2, \dots, \rho_{n_{\text{ele}}}]^T \quad (12a)$$

$$\text{min : } C(\boldsymbol{\rho}) = \mathbf{F}^T \mathbf{U} = \mathbf{U}^T \mathbf{K}(\boldsymbol{\rho}) \mathbf{U} \quad (12b)$$

$$\text{s.t. : } \mathbf{K}(\boldsymbol{\rho}) \mathbf{U} = \mathbf{F} \quad (12c)$$

$$\frac{\sum_{i=1}^{n_{\text{ele}}} v_i \rho_i}{\sum_{i=1}^{n_{\text{ele}}} v_i} \leq f \quad (12d)$$

$$\frac{\sum_{i=1}^{n_{\text{ele}}} \omega_i (\varphi_j) v_i \rho_i}{\sum_{i=1}^{n_{\text{ele}}} v_i} \leq 0, \quad (12e)$$

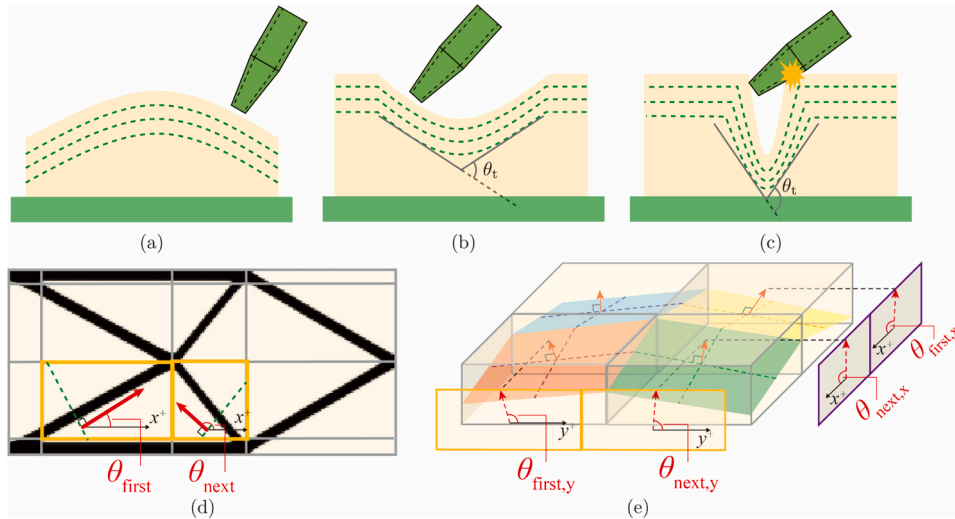


Fig. 7. Effect of surface turning angles: (a) convex printing surfaces show no collision risk; (b) slightly concave surfaces with low turning angle θ_t have a low collision risk; (c) high collision risk is associated with large turning angle θ_t ; (d) in 2D problem, the turning angle θ_t can be determined by the build directions θ_{first} and θ_{next} in adjacent zones; (e) in 3D problems, the turning angle is represented by its projection angles $\theta_{t,x}$ and $\theta_{t,y}$ in the xoz and $yozy$ planes, respectively; $\theta_{t,x}$ can be calculated using $\theta_{\text{first},x}$ and $\theta_{\text{next},x}$, while $\theta_{t,y}$ can be calculated using $\theta_{\text{first},y}$ and $\theta_{\text{next},y}$ (i.e., Equations (10)).

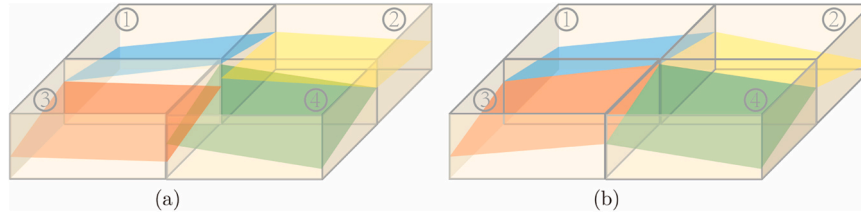


Fig. 8. Printing surface continuity: (a) shows discontinuous printing surfaces, illustrating potential gaps or misalignments; (b) displays continuous printing surfaces, demonstrating seamless transitions and alignments; the circled numbers denote the zone indices.

Note that, in multi-axis AM, for the i th element in the j th zone, its overhang degree ω_i is evaluated by:

$$\omega_i(\theta_{j,x}, \theta_{j,y}) = h(\nabla \rho_i \bullet \lambda(\theta_{j,x}, \theta_{j,y}) - \|\nabla \rho_i\| \bullet \sin(\theta_{\max}) - \xi), \quad (13)$$

where θ_j is the build direction of the j th zone; $\lambda(\theta_{j,x}, \theta_{j,y})$ is the known build direction vector that can be obtained by:

$$\lambda(\theta_{j,x}, \theta_{j,y}) = \left(\frac{1}{\tan(\theta_{j,x})}, \frac{1}{\tan(\theta_{j,y})}, 1 \right) / l_i, \quad (14)$$

$$l_i = \sqrt{\frac{1}{\tan^2(\theta_{j,x})} + \frac{1}{\tan^2(\theta_{j,y})} + 1}, \quad (15)$$

In addition, $h(x) = \frac{1}{1+e^{-20x}}$ represents a Heaviside projection function and ξ is a near 0 constant used to avoid numerical problems. Note that Eq. (13) evaluates the elemental overhang degree by using the intersection angle between the build direction and the density gradient, addressing the less conservative issue for Constraints (7). Since Equations (12) introduces only one additional constraint compared to traditional topology optimisation, we utilise the Method of Moving Asymptotes [50] to efficiently tackle the problem.

4. Numerical examples

In this section, four examples are presented to demonstrate the effectiveness of the proposed approach. In the topology optimisation, the material Young's modulus E_0 and Poisson's ratio ν are 1.0 MPa and 0.3, respectively. The minimum Young's modulus E_{\min} is 1×10^{-9} MPa and the penalty parameter p is taken as 3. As our approach is designed for cases where overhang effects are more significant, we generally use a maximum overhang angle of $\theta_{\max} = 30^\circ$, unless stated otherwise. This value corresponds to the overhang angle for metal AM, which is lower than the commonly used $\theta_{\max} = 45^\circ$ for plastic AM. All design domains are meshed using hexahedral elements. The maximum turning angle

$\theta_{t,\max}$ is 30° . The finite element analysis is carried out by ABAQUS [51]. For comparison, the compliance values of the multi-axis-based solutions are evaluated against two benchmark sets. The first set consists of nominal solutions obtained from traditional topology optimisation, which serve as strict lower-bound cases without overhang constraints. Therefore, the compliance increase relative to these nominal solutions is used to quantify the performance reduction resulting from the integration of overhang constraints. The second set includes solutions optimised with 3-axis-based overhang constraints, which demonstrate the benefits of incorporating the multi-axis system.

4.1. 3D joint

The approach is first examined using a simple 3D joint example shown in Fig. 9(a), where F represents a unit load. The design domain dimensions are $L = 20$ mm, $D = H = 60$ mm, and the assumed volume fraction $f = 0.1$. The optimised solution from the traditional SIMP method is shown in Fig. 9(b), with a compliance value of $C = 252.37$ N • mm. To eliminate zigzag boundaries, the optimised structure is further smoothed using the PolyNURBS tools in Altair Inspire, as shown in Fig. 9(c). When 3-axis AM is considered, the unprintable proportion r_{unp} is 13.2 % when $\theta_{\max} = 30^\circ$. Therefore, multi-axis AM can be utilised to improve printability.

The multi-axis AM-based approach begins with the optimised solution in Fig. 9(c). Firstly, the design domain is subdivided into 72 zones in a $2 \times 6 \times 6$ configuration, as shown in Fig. 10(a). The optimisation problem, expressed by Equations (8), is then solved to determine the local build directions, utilising the optimised structure as input constant. With the local build directions determined, the printing surfaces can be constructed, being orthogonal to the build directions, as shown in Fig. 10 (b-2). Despite the improved printability from the identified printing surfaces, 7.5 % of the structure remains unprintable. Hence, the re-optimisation step, expressed by Equations (12), is carried out. In contrast to the build direction optimisation problem (i.e., Equations (8)), re-optimisation redesigns the structure while maintaining the printing

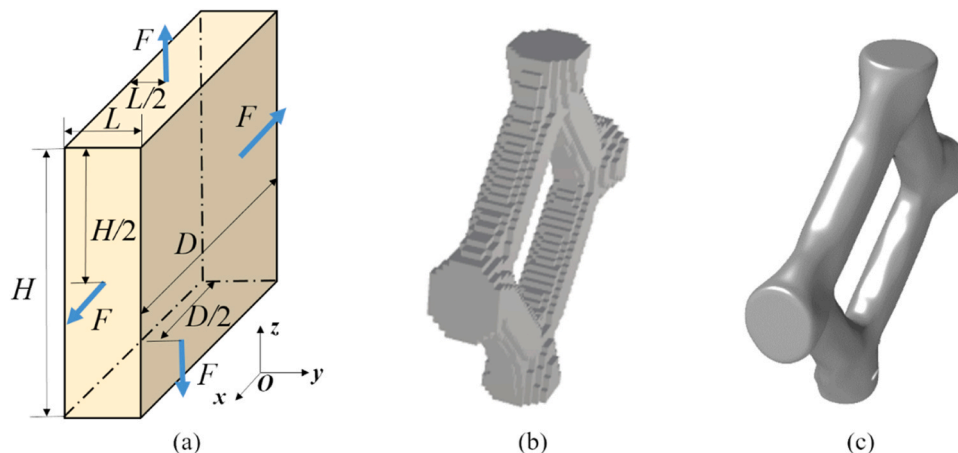


Fig. 9. 3D joint example: (a) problem description; (b) solution from the traditional topology optimisation approach; (c) smoothed structure.

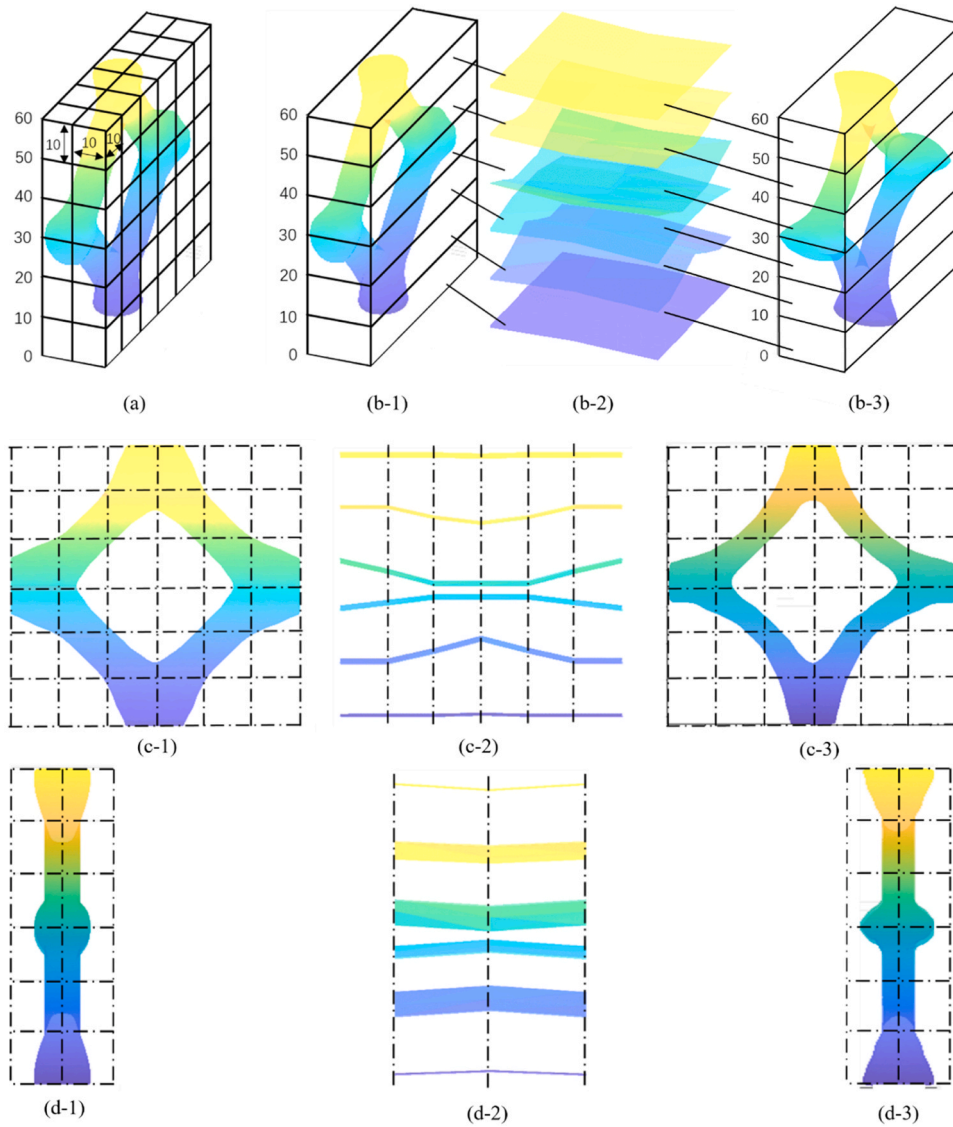


Fig. 10. Optimised results of the 3D joint problem; (a) zone subdivision; (b) two-step optimisation, where (b-1) structural topology from traditional topology optimisation; (b-2) optimised printing surface; (b-3) structural topology after re-optimisation; (c) and (d) show front and side view graphs of the optimised solutions in (b-3), respectively; the structural parts and the corresponding printing surfaces at the same elevation are colored consistently to indicate their association.

surface constant. The obtained solution, shown in Fig. 10(b-3), reduces the unprintable portion to zero and causes only a 3.2 % increase in compliance compared to the original structure in Fig. 9(c), which

demonstrates the effectiveness of the proposed approach. The front and side views of the optimised structures and printing surfaces are shown in Fig. 10(c) and (d). Following re-optimisation, the 3D joint preserves its

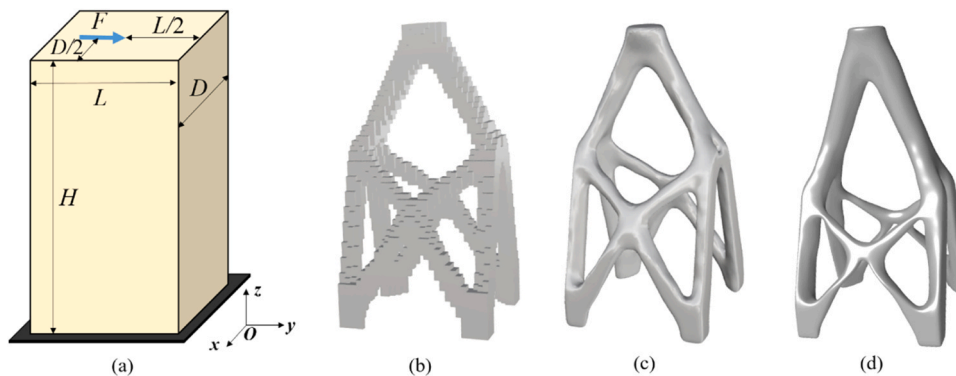


Fig. 11. Topology optimisation of a 3D cantilever; (a) design domain; (b) solution from the traditional topology optimisation; (c) smoothed structure; (d) optimised solution with overhang constraints based on 3-axis AM.

four-member skeleton, with local geometries fine-tuned to avoid overhangs, resulting in a minor increase in compliance.

4.2. 3D cantilever

To illustrate the robustness of the proposed approach, this section presents a more complex 3D cantilever example. The maximum overhang angle θ_{max} is set to 30° . The problem description is in Fig. 11(a), with the design domain dimensions of $30\text{ mm} \times 30\text{ mm} \times 60\text{ mm}$. A load of $F = 5\text{ N}$ is applied to the midpoint of the top surface. The volume fraction f is taken as 0.15. The solution from the traditional SIMP approach and the smoothed solution are shown in Fig. 11(b) and (c), respectively, with a compliance value of $C = 942.52\text{ N} \bullet \text{mm}$. For

comparison purpose, we compute an overhang-free solution based on 3-axis AM, by using planar printing surfaces in the re-optimisation step, as shown in Fig. 11(d). The overall compliance is $1148.84\text{ N} \bullet \text{mm}$, which causes an approximately 21.89% sacrifice on the structural performance (relative to Fig. 11(c)).

Similar to the 3D joint structure, the design domain is subdivided into $3 \times 3 \times 6$ zones, as shown in Fig. 12(a). With 3-axis AM, there are 696 unprintable boundary elements, resulting in an 11.4% unprintable ratio, which significantly exceeds the target threshold of 1%. After optimising the local printing directions, the printing surfaces are shown in Fig. 12(b-2). The number of unprintable boundary elements is reduced to 452, bringing the unprintable ratio down to 7.4%. Since the unprintable ratio still surpasses the target threshold of 1%, further re-

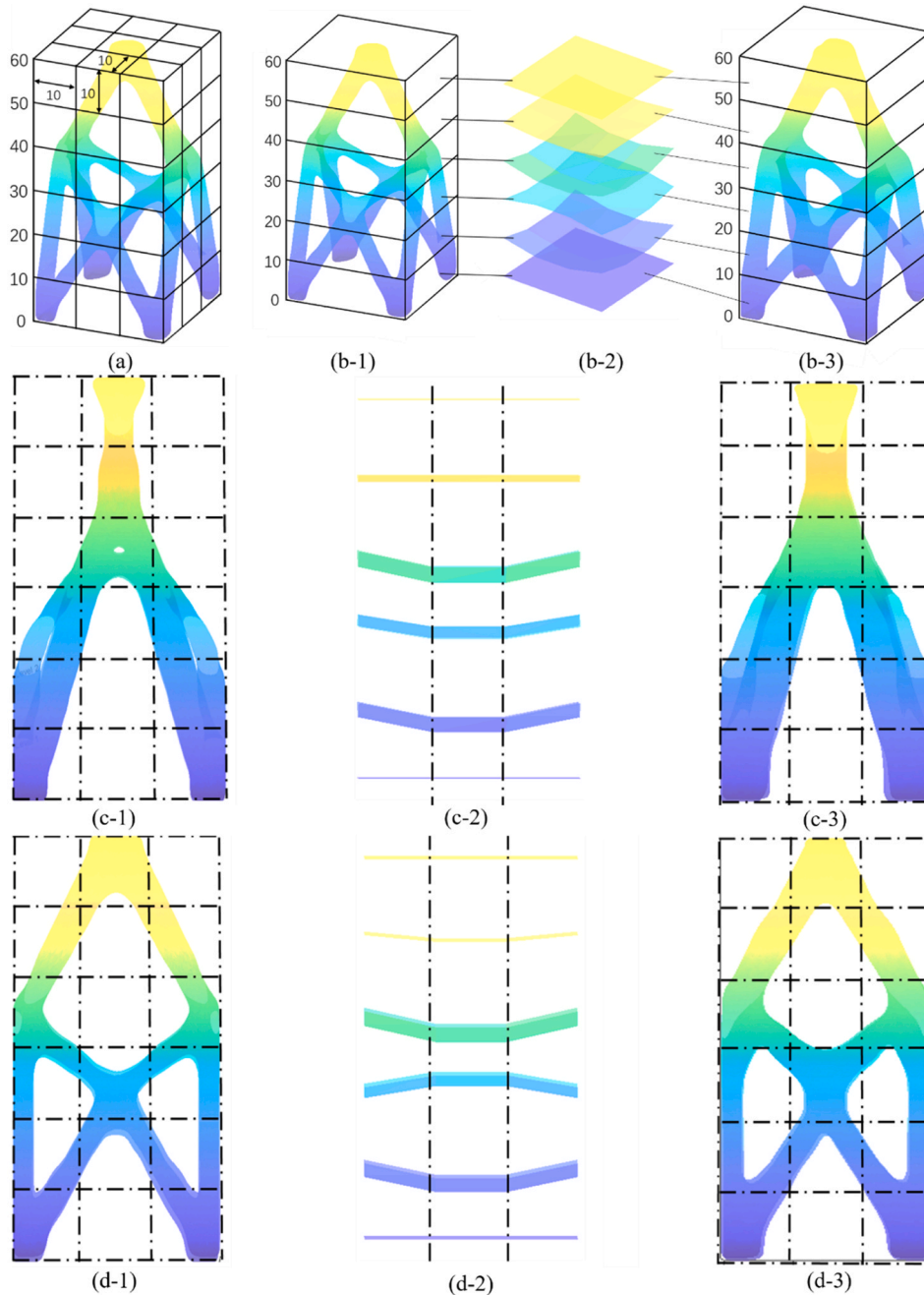


Fig. 12. Optimised results of the 3D cantilever example; (a) zone subdivision; (b) two-step optimisation, where (b-1) structural topology from traditional topology optimisation; (b-2) optimised printing surface; (b-3) structural topology after re-optimisation; (c) and (d) show front and side view graphs of the optimised solutions in (b), respectively; the structural parts and the corresponding printing surfaces at the same elevation are colored consistently to indicate their association.

optimisation is necessary. The structure from the re-optimisation step is shown in Fig. 12(b-3). At this stage, the unprintable proportion of the structure boundary is reduced to 0 %, while the overall compliance of the structure increases from 942.52 N • mm to 984.15 N • mm, indicating a performance sacrifice of 4.4 %, significantly lower than the 3-axis-based solution in Fig. 11(d). The front and side view graphs in Fig. 12(c) and (d) demonstrate that with the superior flexibility of multi-axis AM, the structural geometry is only slightly adjusted, maintaining the skeleton of the entire structure.

4.3. 3D wheel

In this section, we apply the multi-axis optimisation approach to the 3D wheel example as shown in Fig. 13(a). The size of design domain is $L = H = D = 60$ mm, with the volume fraction as 0.15. A vertical load of $F = 5$ N is applied at the midpoint of the bottom surface. The optimised solution with $C = 881.28$ N • mm is shown in Fig. 13(b). The maximum overhang angle θ_{\max} is taken as 45° . After the optimisation for 3-axis AM in Fig. 13(c), the compliance value is 1016.11 N • mm, exhibits a sacrifice of 15.3 % on structural performance.

The zone arrangement is illustrated in Fig. 14(a). Initially, the unprintable proportion is 15.5 % under 3-axis AM. By optimising the surfaces for multi-axis additive manufacturing (as shown in Fig. 14(c)), the unprintable ratio is reduced to 10.5 %. In the printing plan optimisation, the printing surfaces in zones above an elevation of 40 mm are set as planar due to the absence of structures in those regions. During the re-optimisation stage, the influence of height constraints is examined by limiting the structure height to 40 mm, 50 mm, and 60 mm, achieved by imposing corresponding non-designable domains at the top. The resulting solutions from the re-optimisation are presented in Fig. 14(d) and (e). When the structural heights are limited to 40 mm, 50 mm, and 60 mm, the corresponding compliance increases are 7.6 %, 5.3 %, and 1.4 %, respectively. This outcome aligns with expectations. As the overhang constraint is geometry-dependent, allowing more height provides the algorithm with greater design freedom to adjust the structure, resulting in overhang-free structures with lower compliance values.

4.4. The influence of the maximum overhang angle

The maximum overhang angle is a crucial AM parameter. To examine its influence, a 3D beam example is utilised in this section. The example description is in Fig. 15(a), and the design domain dimensions are $L = 120$ mm, $H = 30$ mm, and $D = 30$ mm, respectively. A unit load F is applied at the midpoint of the bottom surface; and the volume fraction $f = 0.20$. The optimised structure from the traditional SIMP approach is in Fig. 15(b), with a compliance value of $C = 1357.62$ N • mm. The study tests three maximum overhang angles θ_{\max} : 60° , 45° and 30° .

The zone size is taken as 10 mm \times 10 mm \times 10 mm, as shown in the domain subdivision graph in Fig. 16(a). By taking advantage of the symmetry, half of the problem is considered, as shown in Fig. 16(b). The

structure contains 5368 boundary elements; and in 3-axis AM, the unprintable ratios correspond to three θ_{\max} values are 9.9 %, 12.7 % and 24.6 %, respectively. With the multi-axis optimised build directions (as shown in Fig. 17(b)) applied, the unprintable ratios are reduced to 7.2 %, 10.2 % and 16.1 %, respectively. It is evident that as the maximum overhang angle decreases, the unprintable ratio increases accordingly. Nevertheless, after the re-optimisation, the unprintable elements are eliminated for all three cases (Fig. 18). The compliance values are increased to 1390.42 N • mm, 1452.68 N • mm and 1466.37 N • mm, resulting in performance sacrifice values of 2.4 %, 7.0 %, and 8.0 %, respectively, all of which are under 10 %.

The convergence history of the re-optimisation step with $\theta_{\max} = 30^\circ$ is shown in Fig. 19. The compliance value decreases rapidly at the first step and then it takes another 74 iterations to reach a final convergence.

For comparison, the three problems shown in Fig. 18 were solved with overhang constraints based on 3-axis AM, with the resulting solutions displayed in Fig. 20. The compliance increases for the solutions in Fig. 20(a-c) relative to Fig. 15(b) are 10.70 %, 14.15 %, and 18.68 %, respectively. These increases are all higher than those obtained with the multi-axis AM approach, highlighting the effectiveness of the proposed method.

4.5. The influence of the zone size

The zone size is another important parameter in the printing plan optimisation. Therefore, in this section, the same 3D beam in Section 4.4 is used to examine the influence of zone size. As shown in Fig. 21, three different zone sizes are tested: 15 mm \times 15 mm \times 15 mm, 10 mm \times 10 mm \times 10 mm and 5 mm \times 5 mm \times 5 mm. The maximum overhang angle is taken as $\theta_{\max} = 45^\circ$. After the local printing directions are identified, the unprintable elements in the three cases are 971, 863, and 651, respectively. Following re-optimisation, the unprintable ratio is reduced to zero for all three cases, and the compliance values increase to 1490.65 N • mm, 1466.37 N • mm, and 1452.79 N • mm, respectively. Side view graphs of the optimised results are shown in Fig. 22. Compared to Fig. 16(b), these represent increases in compliance of 9.80 %, 7.98 %, and 7.01 %, respectively. The results show that finer zone subdivisions introduce additional design freedom to the printing surfaces, resulting in lower compliance values after re-optimisation.

5. Print validation

In this section, we validate the optimised results first through a numerical printing simulation using the VERICUT software. With the optimised printing surfaces identified, the printing process begins with Layer 1 located at the bottom and progresses upward, completing each layer sequentially, as illustrated in Fig. 23. It is important to note that the print nozzle is assumed to remain vertical throughout the process, while the printing platform rotates to align with the optimised printing surfaces and adjusts the component's orientation relative to gravity, effectively addressing the overhang problem.

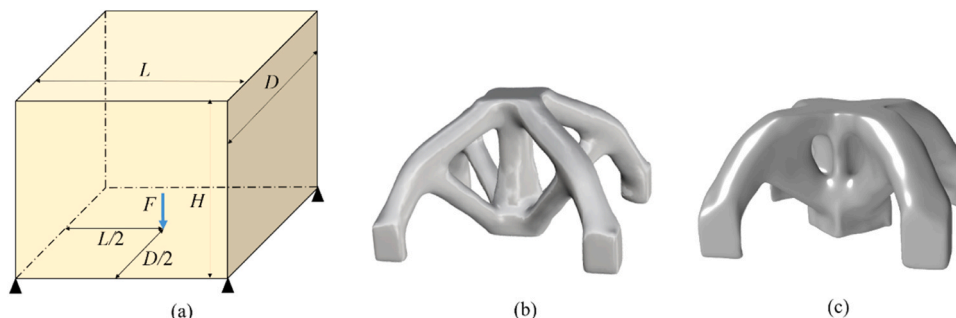


Fig. 13. 3D wheel example: (a) description of the problem; (b) smoothed structure; (c) solutions from the optimisation for 3-axis AM.

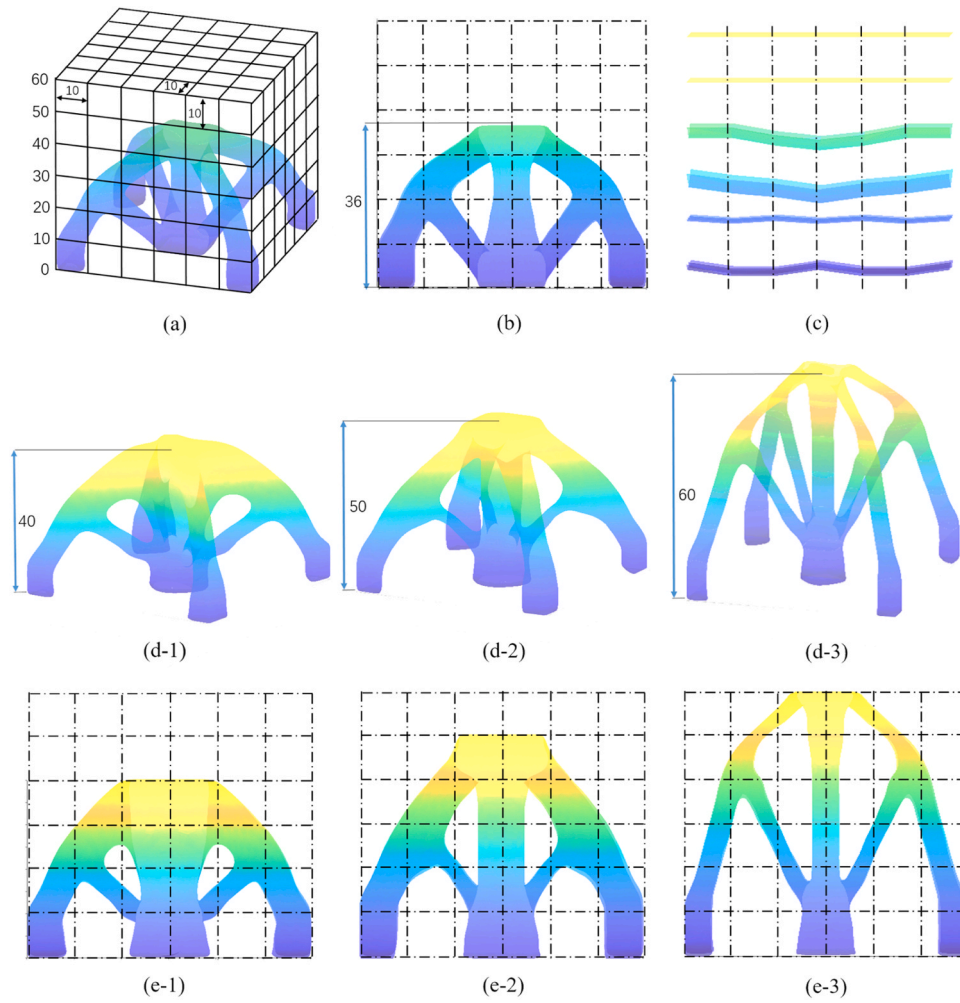


Fig. 14. Optimised results of the 3D wheel problem; (a) zone subdivision; (b) front view of the solution from the traditional topology optimisation approach; (c) front view of the optimised printing surfaces; (d) optimised overhang-free structures with different height limits, where the domain height is constrained to (1) 40 mm, (2) 50 mm, and (3) 60 mm, with corresponding compliance values of (1) 948.26 N-mm, (2) 927.98 N-mm, and (3) 893.62 N-mm; (e) front view of the optimised solutions in (d); the structural parts and the corresponding printing surfaces at the same elevation are colored consistently to indicate their association.

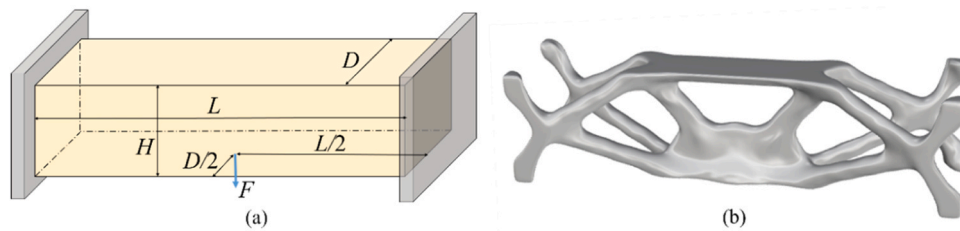


Fig. 15. 3D beam example; (a) design domain; (b) smoothed structure.

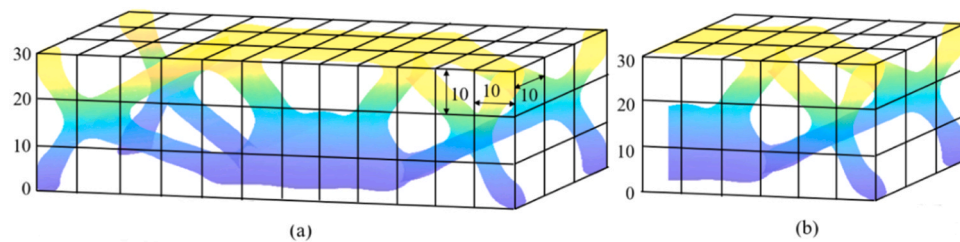


Fig. 16. Subdivision of the 3D beam example; (a) full problem; (b) half problem.

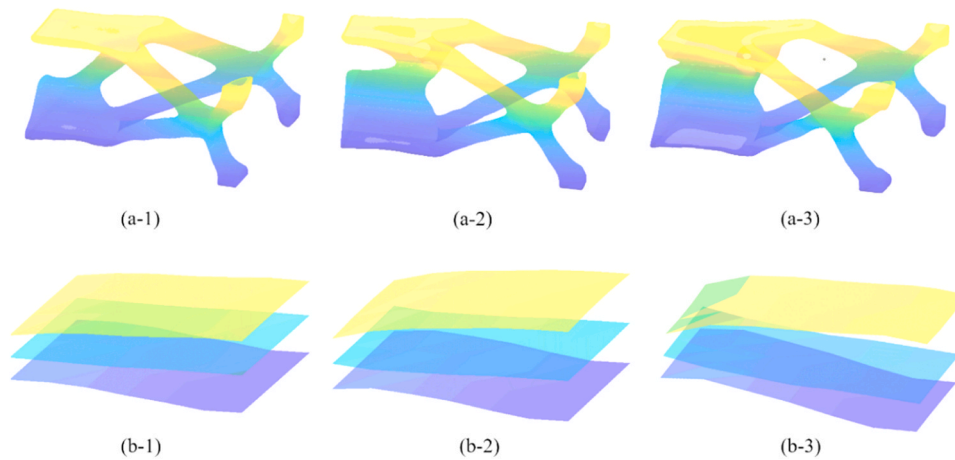


Fig. 17. Optimised solutions for the 3D beam example; (a) solutions from the re-optimisation step; (b) the optimised printing surfaces; the maximum overhang angle θ_{max} are 60° , 45° and 30° for solutions in (1), (2) and (3), respectively; the structural parts and the corresponding printing surfaces at the same elevation are colored consistently to indicate their association.

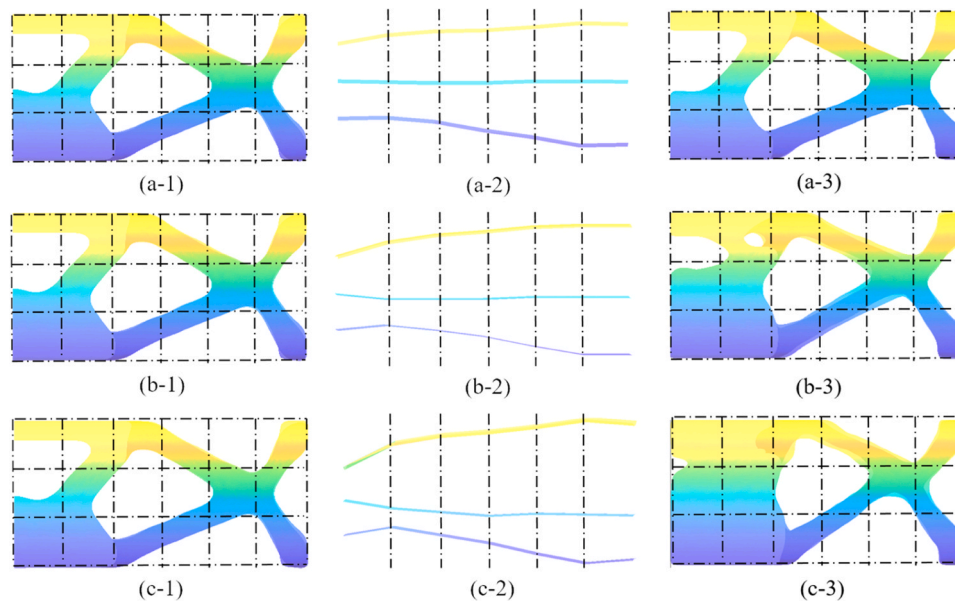


Fig. 18. Side view graphs of the solutions in Fig. 17: (1) structures from the traditional topology optimisation; (2) optimised printing surfaces; (3) structures from the re-optimisation step; the maximum overhang angles θ_{max} are set at 60° , 45° and 30° for solutions in (a), (b) and (c), respectively; the structural parts and the corresponding printing surfaces at the same elevation are colored consistently to indicate their association.

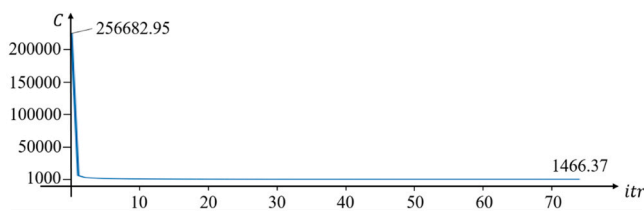


Fig. 19. The convergence history of re-optimisation case for Fig. 18 (c).

Within each layer, the tool path is established by first slicing the structure along the optimised surfaces to derive the component's contour path. This contour is then filled with a zigzag pattern, as shown in Fig. 24. Both the contour and infill paths comprise the complete printing tool path used during the manufacturing process.

The printing path simulation employs VERICUT with the BeAM magic 2.0 5-axis machine shown in Fig. 25. Printing paths of the

optimised 3D cantilever, the 3D wheel and the 3D beam are generated and simulated. It is important to note that, unlike 3-axis AM, multi-axis AM carries a risk of collision between the printing nozzle and the already printed component. To mitigate this risk, a turning angle constraint, as described in Section 3.2, is employed. In all VERICUT simulations, no collisions were detected, demonstrating the effectiveness of the turning angle constraint in preventing such issues. Videos of the simulations can be found in the GitHub repository linked in the Supplementary videos section.

Besides the numerical validation using VERICUT, the 3D cantilever is physically printed using a multi-axis Wire Arc Additive Manufacturing (WAAM) machine shown in Fig. 26. The structure model is scaled to $180 \text{ mm} \times 180 \text{ mm} \times 360 \text{ mm}$. A commercial 316 L stainless steel plate with dimensions of $400 \text{ mm} \times 400 \text{ mm} \times 20 \text{ mm}$ was used as the substrate and was polished and cleaned before the deposition process. The raw material used was a 1.2 mm diameter 316 L stainless steel wire. The optimised structure was deposited using the Cold Metal Transfer (CMT)

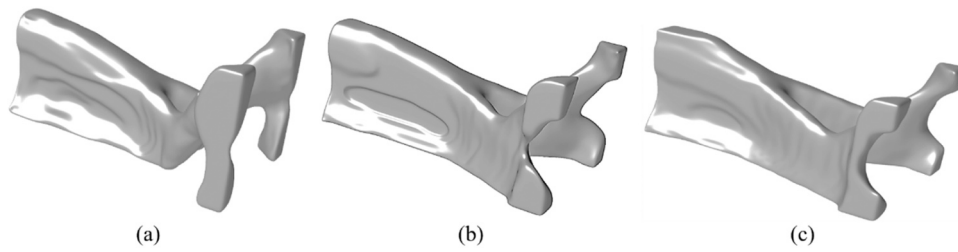


Fig. 20. The solutions from the approach for 3-axis AM, where (a) $\theta_{\max} = 60^\circ$ and $C = 1502.89 \text{ N} \cdot \text{mm}$; (b) $\theta_{\max} = 45^\circ$ and $C = 1549.13 \text{ N} \cdot \text{mm}$; (c) $\theta_{\max} = 30^\circ$ and $C = 1611.34 \text{ N} \cdot \text{mm}$; θ_{\max} and C represent the maximum overhang angle and the structural compliance, respectively;.

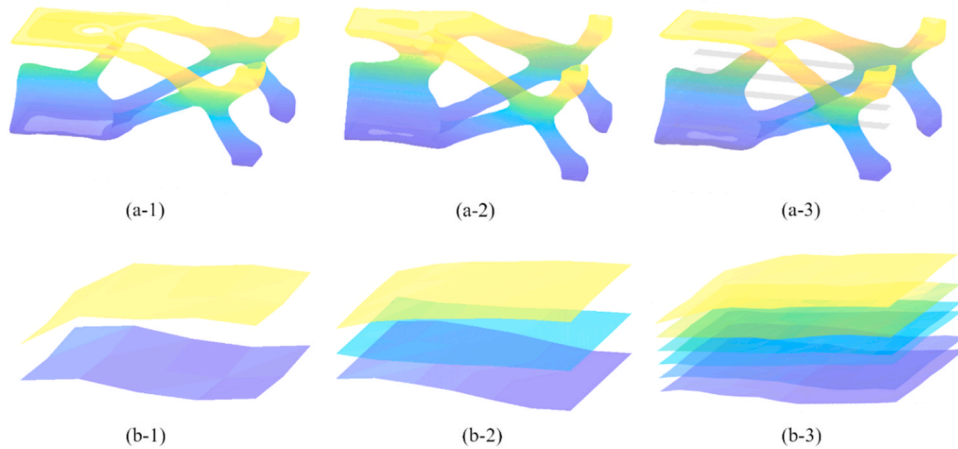


Fig. 21. Optimised solutions for the 3D beam example; (a) solutions from the re-optimisation step; (b) the optimised printing surfaces; the zone sizes are $15 \text{ mm} \times 15 \text{ mm} \times 15 \text{ mm}$; $10 \text{ mm} \times 10 \text{ mm} \times 10 \text{ mm}$ and $5 \text{ mm} \times 5 \text{ mm} \times 5 \text{ mm}$ for solutions in (1), (2) and (3), respectively; the structural parts and the corresponding printing surfaces at the same elevation are colored consistently to indicate their association.

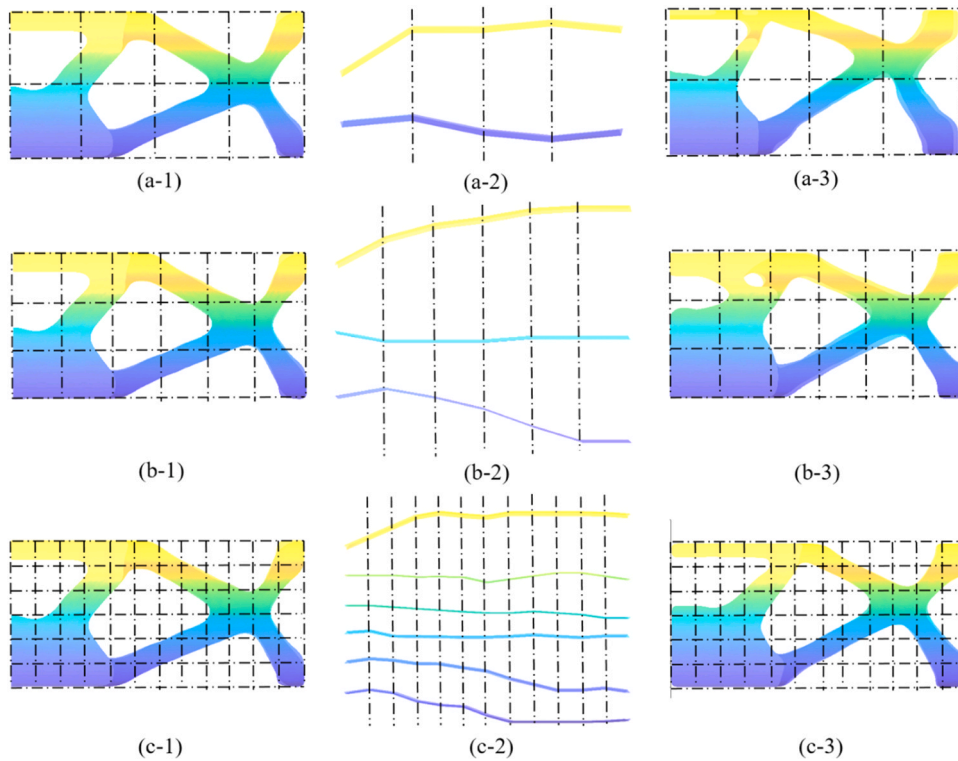


Fig. 22. Side view graphs of the solutions in Fig. 21: (1) structures from the traditional topology optimisation; (2) optimised printing surfaces; (3) structures from the re-optimisation step; the zone sizes are $15 \text{ mm} \times 15 \text{ mm} \times 15 \text{ mm}$; $10 \text{ mm} \times 10 \text{ mm} \times 10 \text{ mm}$ and $5 \text{ mm} \times 5 \text{ mm} \times 5 \text{ mm}$ for solutions in (a), (b) and (c), respectively; the structural parts and the corresponding printing surfaces at the same elevation are colored consistently to indicate their association.

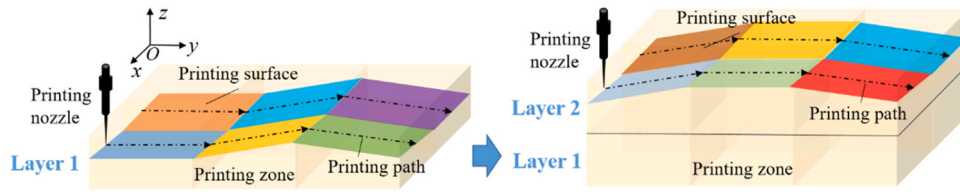


Fig. 23. Printing sequences based on the optimised multi-axis printing surfaces.

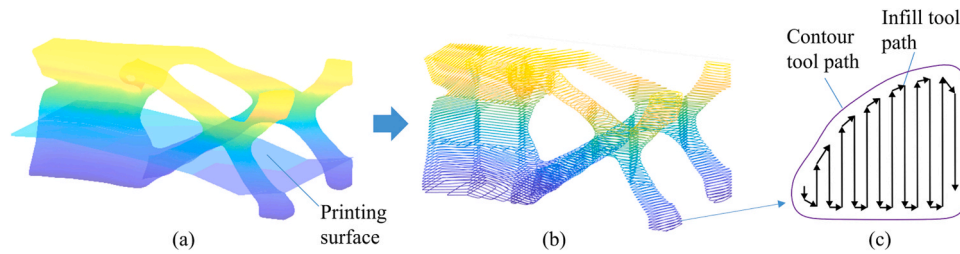


Fig. 24. The process of generating tool path; (a) the structure and the printing surface; (b) slicing results; (c) infilling slice with zigzag tool path.

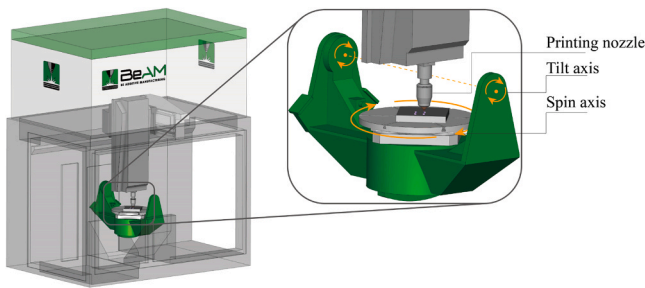


Fig. 25. The BeAM magic 2.0 machine used in the VERICUT simulation.

technology. Printing parameters including print speed, wire feed rate, etc. are shown in Table 1.

Photos of several intermediate printing states are displayed in Fig. 27, while the final printed model is presented in Fig. 28. In addition, three intermediate clips of the printing process are available in the GitHub repository linked in the Supplementary videos section. The layer thickness used varies between 1.75 mm and 2.50 mm. A strategy similar to [52] is adopted to tailor the layer thickness for each zone, ensuring the continuity of the curved printing surfaces.

To mitigate the overhang effect on the inclined members, optimised printing surfaces from Fig. 12 were employed, resulting in inclined printing layers as shown in Fig. 28. Notably, the orientation of the model was dynamically adjusted using the rotatable base platform, while the printing nozzle remained vertical throughout the process. Furthermore, no collisions occurred during the entire printing process, affirming the

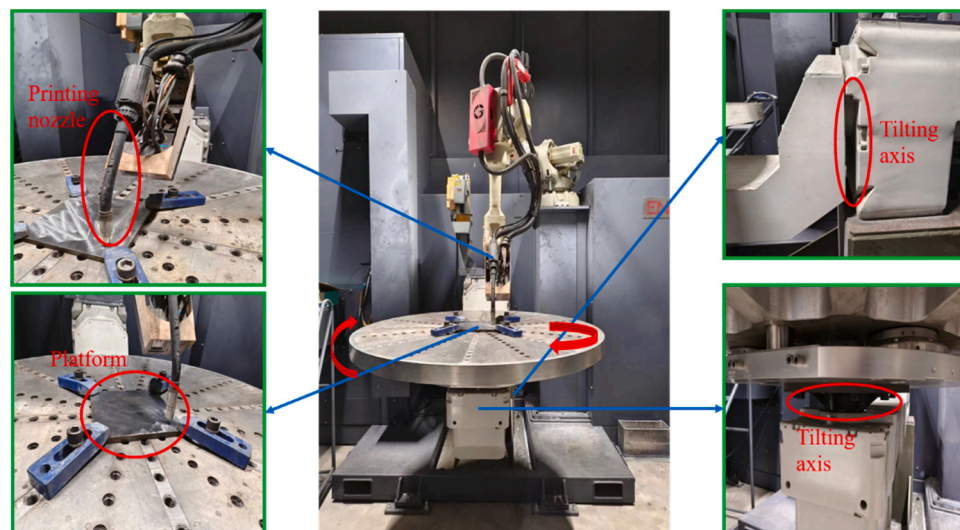


Fig. 26. Multi-axis WAAM machine with rotatable base platform.

Table 1
WAAM printing parameters.

Print speed (mm/s)	Wire feed rate (m/min)	Voltage (V)	Current (A)	Start current (A)	End current (A)	Start arc time (s)	End arc time (s)
11	5.4	13.1	147	153	119	0.3	0.6

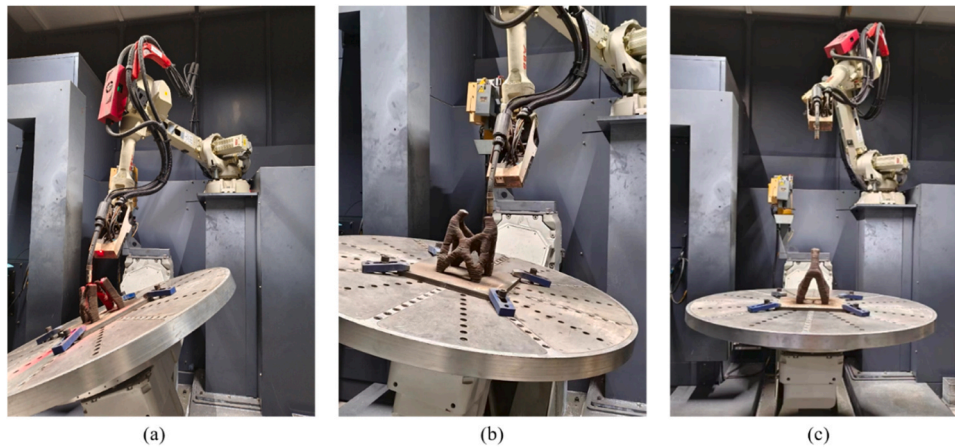


Fig. 27. Multi-axis printing procedure of the 3D stainless steel cantilever using a WAAM machine.

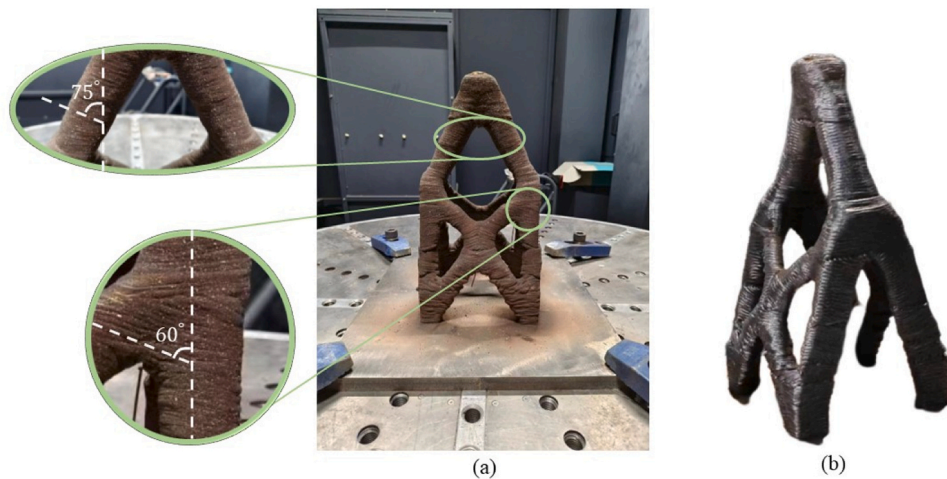


Fig. 28. Physical model of the 3D cantilever: (a) printed model with inclined printing layers to overcome overhang; (b) structure processed with sandblasting.

effectiveness of the collision constraints outlined in Equations (10). However, the surface of the printed component is relatively rough, as WAAM, while offering faster printing speeds compared to other DED techniques, produces a larger bead width that reduces surface quality. Minor misalignments were also observed at the interfaces between zone layers (e.g., between Layer 1 and Layer 2 in Fig. 23) due to abrupt changes in local build directions at these points. Nevertheless, these did not significantly impact the structural formation and the misalignment issue could be further mitigated in future studies by locally adjusting the printing tool path to account for changes in build directions.

It is worth noting that two key challenges were encountered during the printing process. First, the large bead width inherent to the WAAM technique, while enabling faster printing speeds compared to other DED methods [52], makes it unsuitable for structures with thin elements (e.g., Fig. 14(d-3) and Fig. 17(a-3)). Second, thermal deformation in metal AM becomes more pronounced when more build direction zones are utilised, leading to variations in local build accuracy. In future work, the first issue could be addressed by incorporating length-scale constraints to limit element size [16], and the second by introducing constraints related to residual stress [53]. Nevertheless, these challenges are specific to metal AM and are less likely to arise in plastic multi-axis AM. In addition, despite these issues, the effectiveness of the proposed approach in addressing the overhang problem has been successfully validated using the cantilever example.

6. Conclusion

In this paper, we propose a novel two-step optimisation approach to design self-supportable 3D structures using multi-axis additive manufacturing (multi-axis AM). In the first step, an optimised structure from the traditional topology optimisation is employed as the starting point for a printing plan optimisation problem, which identifies multi-axis printing surfaces that maximise the printable proportion of the structure. However, as the structure remains constant in the first step, the identified multi-axis printing surfaces cannot ensure complete printability. Consequently, a second re-optimisation step is implemented to further address the overhang issue by adjusting the structure topology. To demonstrate the efficacy of our approach, we present four numerical optimisation examples, supplemented by both numerical and physical printing validations. These efforts lead to the following conclusions:

1. Compared with benchmark results from the traditional topology optimisation approaches, the overhang-free requirement results in a decrease in structural stiffness. However, the high flexibility of multi-axis AM effectively limits this decrease, with a maximum stiffness drop capped at 9.80 % in all examined cases.
2. The regular grid approach for domain subdivision demonstrates robustness and versatility across various optimisation scenarios. Smaller zone sizes typically yield more satisfactory solutions compared to larger ones. For instance, in the cantilever example,

reducing the zone size from 15 mm × 15 mm × 15 mm to 5 mm × 5 mm × 5 mm resulted in a decrease in performance sacrifices from 9.80 % to 7.01 %.

3. Imposing constraints on the turning angle has proven effective in reducing the risk of collisions. During the numerical printing simulations with VERICUT and physical printing validations using a multi-axis WAAM machine, no collisions were detected throughout the printing process.

In summary, this study presents a powerful tool for designing and manufacturing topology-optimised structures without the need for support structures. The benefits are particularly pronounced in metal AM, where it reduces material waste and eliminates post-processing associated with support removal. This advancement improves the efficiency and practicality of additive manufacturing technologies in industrial applications, promoting innovation and encouraging broader adoption within the field.

CRedit authorship contribution statement

Yang Zhao: Writing – review & editing, Methodology, Investigation, Funding acquisition. **Yi Min Xie:** Writing – review & editing, Methodology, Funding acquisition. **Guan Quan:** Writing – review & editing, Methodology, Investigation, Funding acquisition. **Zhen Wang:** Writing – review & editing, Methodology, Investigation. **Jun Ye:** Writing – review & editing, Methodology, Investigation, Funding acquisition. **Hongjia Lu:** Writing – review & editing, Visualization, Software, Methodology, Investigation. **Qichen Guo:** Writing – original draft, Visualization, Software, Methodology, Investigation.

Declaration of Competing Interest

The authors declare that they have no known competing financial interests or personal relationships that could have appeared to influence the work reported in this paper.

Acknowledgements

The authors would like to acknowledge the financial support to this project by the National Natural Science Foundation of China (No. 52078452, 52208215), the Basic Public Research Project of Zhejiang Province (No. LGG22E080005, LQ22E080008) and the Australian Research Council (No. FL190100014).

Supplementary videos

The supplementary videos can be found in the following GitHub repository:

https://github.com/CHENDLUT/Opt_with_multi-axis_AM_2024

Data availability

Data will be made available on request.

References

- [1] E. Andreassen, A. Clausen, M. Schevenels, B. Lazarov, O. Sigmund, Efficient topology optimization in MATLAB using 88 lines of code, *Struct. Multidiscip. Optim.* 43 (2011) 1–16, <https://doi.org/10.1007/s00158-010-0594-7>.
- [2] M. Bendsoe, O. Sigmund, *Topology Optimization: Theory, Method and Applications*, Springer Science & Business Media, 2003.
- [3] M.P. Bendsoe, N. Kikuchi, Generating optimal topologies in structural design using a homogenization method, *Comput. Methods Appl. Mech. Eng.* 71 (2) (1988) 197–224, [https://doi.org/10.1016/0045-7825\(88\)90086-2](https://doi.org/10.1016/0045-7825(88)90086-2).
- [4] X. Huang, Y.M. Xie, Bidirectional evolutionary topology optimization for structures with geometrical and material nonlinearities, *AIAA journal* 45 (2007) 308–313, <https://doi.org/10.2514/1.25046>.
- [5] J. Ye, P. Kyvelou, F. Gilardi, H. Lu, M. Gilbert, L. Gardner, An end-to-end framework for the additive manufacture of optimized tubular structures, *IEEE Access* 9 (2021) 165476–165489, <https://doi.org/10.1109/ACCESS.2021.3132797>.
- [6] A.A. Zadpoor, Design for additive bio-manufacturing: from patient-specific medical devices to rationally designed meta-biomaterials, *Int. J. Mol. Sci.* 18 (8) (2017) 1607, <https://doi.org/10.3390/ijms18081607>.
- [7] E. Garner, H.M.A. Kolken, C.C.L. Wang, A.A. Zadpoor, J. Wu, Compatibility in microstructural optimization for additive manufacturing, *Addit. Manuf.* 26 (2019) 65–75, <https://doi.org/10.1016/j.addma.2018.12.007>.
- [8] P. Stavropoulos, *Additive Manufacturing: Design, Processes and Applications*, Springer Nature, 2023, <https://doi.org/10.1007/978-3-031-33793-2>.
- [9] H. Wang, W. Du, Y. Zhao, Y. Wang, R. Hao, M. Yang, Joints for treelike column structures based on generative design and additive manufacturing, *J. Constr. Steel Res.* 184 (2021) 106794, <https://doi.org/10.1016/j.jcsr.2021.106794>.
- [10] S. Galjaard, S. Hofman, S. Ren, New Opportunities to Optimize Structural Designs in Metal by Using Additive Manufacturing, *Advances in Architectural Geometry 2014*, Springer International Publishing, Cham, 2015, pp. 79–93, https://doi.org/10.1007/978-3-319-11418-7_6.
- [11] H. Strauß, A.G. Emmer Pfenninger Partner, U. Knaack, Additive manufacturing for future facades: the potential of 3D printed parts for the building envelope, *J. Facade Des. Eng.* 3 (2015) 225–235, <https://doi.org/10.3233/FDE-150042>.
- [12] B. Waldschmitt, C.B. Costanzi, U. Knaack, J. Lange, 3D printing of column structures for architectural applications, *Archit. Struct. Constr.* 2 (4) (2022) 565–574, <https://doi.org/10.1007/s44150-022-00050-z>.
- [13] V. Laghi, M. Palermo, G. Gasparini, T. Trombetti, Computational design and manufacturing of a half-scaled 3D-printed stainless steel diaphragm column, *Addit. Manuf.* 36 (2020) 101505, <https://doi.org/10.1016/j.addma.2020.101505>.
- [14] T. Feucht, B. Waldschmitt, J. Lange, M. Erven, 3D-printing with steel: additive manufacturing of a bridge in situ, *ce/Pap. 4* (2021) 1695–1701, <https://doi.org/10.1002/cepa.1475>.
- [15] S.Anderson Goehrke, 3D printed steel pedestrian bridge will soon span an Amsterdam canal, *3D Print* (2015). URL: <<https://3dprint.com/72682/amsterdam-3d-printed-bridge/>>
- [16] M. Zhou, B.S. Lazarov, F. Wang, O. Sigmund, Minimum length scale in topology optimization by geometric constraints, *Comput. Methods Appl. Mech. Eng.* 293 (2015) 266–282, <https://doi.org/10.1016/j.cma.2015.05.003>.
- [17] H.Y. Lee, M. Zhu, J.K. Guest, Topology optimization considering multi-axis machining constraints using projection methods, *Comput. Methods Appl. Mech. Eng.* 390 (2022) 114464, <https://doi.org/10.1016/j.cma.2021.114464>.
- [18] Q. Li, W. Chen, S. Liu, L. Tong, Structural topology optimization considering connectivity constraint, *Struct. Multidiscip. Optim.* 54 (4) (2016) 971–984, <https://doi.org/10.1007/s00158-016-1459-5>.
- [19] A.K. Lianos, H. Bikas, P. Stavropoulos, A shape optimization method for part design derived from the buildability restrictions of the directed energy deposition additive manufacturing process, *Designs* 4 (3) (2020) 19, <https://doi.org/10.3390/designs4030019>.
- [20] X. Gu, Q. Yu, Y. Dong, S. He, J. Qu, Structural topology optimization for additive manufacturing with free choice of self-supporting and infill-supporting structures, *Comput. Methods Appl. Mech. Eng.* 421 (2024) 116788, <https://doi.org/10.1016/j.cma.2024.116788>.
- [21] H. Bikas, M.A. Terzakis, P. Stavropoulos, Manufacturability-based design optimization for directed energy deposition processes, *Machines* 2023 11 (9) (2023) 879, <https://doi.org/10.3390/machines11090879>.
- [22] P. Stavropoulos, P. Foteinopoulos, A. Papacharalampopoulos, H. Bikas, Addressing the challenges for the industrial application of additive manufacturing: towards a hybrid solution, *Int. J. Lightweight Mater. Manuf.* 1 (3) (2018) 157–168, <https://doi.org/10.1016/j.ijlmm.2018.07.002>.
- [23] M. Bi, P. Tran, L. Xia, G. Ma, Y.M. Xie, Topology optimization for 3D concrete printing with various manufacturing constraints, *Addit. Manuf.* 57 (2022) 102982, <https://doi.org/10.1016/j.addma.2022.102982>.
- [24] W. Gao, Y. Zhang, D. Ramanujan, K. Ramani, Y. Chen, C.B. Williams, C.C.L. Wang, Y.C. Shin, S. Zhang, P.D. Zavattieri, The status, challenges, and future of additive manufacturing in engineering, *Comput. Aided Des.* 69 (2015) 65–89, <https://doi.org/10.1016/j.cad.2015.04.001>.
- [25] J.K. Guest, M. Zhu, Casting and milling restrictions in topology optimization via projection-based algorithms, *International Design Engineering Technical Conferences and Computers and Information in Engineering Conference 45028* (2012).
- [26] D. Wang, Y. Yang, Z. Yi, X. Su, Research on the fabricating quality optimization of the overhanging surface in SLM process, *Int. J. Adv. Manuf. Tech.* 65 (9) (2013) 1471–1484, <https://doi.org/10.1007/s00170-012-4271-4>.
- [27] A.M. Mirzendehtel, M. Behandish, S. Nelaturi, Topology optimization for manufacturing with accessible support structures, *Comput. Aided Des.* 142 (2022) 103117, <https://doi.org/10.1016/j.cad.2021.103117>.
- [28] G. Strano, L. Hao, R.M. Everson, K.E. Evans, A new approach to the design and optimisation of support structures in additive manufacturing, *Int. J. Adv. Manuf. Tech.* 66 (9) (2013) 1247–1254, <https://doi.org/10.1007/s00170-012-4403-x>.
- [29] P. Stavropoulos, K. Tzimanis, T. Souflas, H. Bikas, Knowledge-based manufacturability assessment for optimization of additive manufacturing processes based on automated feature recognition from CAD models, *Int. J. Adv. Manuf. Tech.* 122 (2) (2022) 993–1007, <https://doi.org/10.1007/s00170-022-09948-w>.
- [30] M. Leary, L. Merli, F. Torti, M. Mazur, M. Brandt, Optimal topology for additive manufacture: a method for enabling additive manufacture of support-free optimal structures, *Mater. Des.* 63 (2014) 678–690, <https://doi.org/10.1016/j.matdes.2014.06.015>.

- [31] A.T. Gaynor, J.K. Guest, Topology optimization considering overhang constraints: Eliminating sacrificial support material in additive manufacturing through design, *Struct. Multidiscip. Optim.* 54 (5) (2016) 1157–1172, <https://doi.org/10.1007/s00158-016-1551-x>.
- [32] M. Langelaar, Combined optimization of part topology, support structure layout and build orientation for additive manufacturing, *Struct. Multidiscip. Optim.* 57 (5) (2018) 1985–2004, <https://doi.org/10.1007/s00158-017-1877-z>.
- [33] J. Pellens, G. Lombaert, B. Lazarov, M. Schevenels, Combined length scale and overhang angle control in minimum compliance topology optimization for additive manufacturing, *Struct. Multidiscip. Optim.* 59 (6) (2019) 2005–2022, <https://doi.org/10.1007/s00158-018-2168-z>.
- [34] K. Zhang, G. Cheng, L. Xu, Topology optimization considering overhang constraint in additive manufacturing, *Comput. Struct.* 212 (2019) 86–100, <https://doi.org/10.1016/j.compstruc.2018.10.011>.
- [35] A. Garaigordobil, R. Ansola, J. Santamaría, I. Fernández de Bustos, A new overhang constraint for topology optimization of self-supporting structures in additive manufacturing, *Struct. Multidiscip. Optim.* 58 (5) (2018) 2003–2017, <https://doi.org/10.1007/s00158-018-2010-7>.
- [36] W. Wang, D. Feng, L. Yang, S. Li, C.C.L. Wang, Topology optimization of self-supporting lattice structure, *Addit. Manufact.* 67 (2023) 103507, <https://doi.org/10.1016/j.addma.2023.103507>.
- [37] H. Jiang, Z. He, E. Li, C. Jiang, D. Mi, Additive manufacturing-driven topological design considering overhang and connectivity constraints induced by closed cavity, *Struct. Multidiscip. Optim.* 67 (7) (2024) 118, <https://doi.org/10.1007/s00158-024-03840-9>.
- [38] G. Allaire, C. Dapogny, R. Estevez, A. Faure, G. Michailidis, Structural optimization under overhang constraints imposed by additive manufacturing technologies, *J. Comput. Phys.* 351 (2017) 295–328, <https://doi.org/10.1016/j.jcp.2017.09.041>.
- [39] W. Gao, Y. Zhang, D. Nazzetta, K. Ramani, R. Cipra, *RevoMaker: Enabling Multi-directional and Functionally-embedded 3D printing using a Rotational Cuboidal Platform, Software & Technology, ACM, Charlotte, NC, 2015, pp. 437–446.*
- [40] B.T. Gibson, P. Mhatre, M.C. Borish, C.E. Atkins, J.T. Potter, J.E. Vaughan, L. J. Love, Controls and process planning strategies for 5-axis laser directed energy deposition of Ti-6Al-4V using an 8-axis industrial robot and rotary motion, *Addit. Manufact.* 58 (2022) 103048, <https://doi.org/10.1016/j.addma.2022.103048>.
- [41] C. Wu, C. Dai, G. Fang, Y.-J. Liu, C.C.L. Wang, Automation, RoboFDM: A robotic system for support-free fabrication using FDM, *IEEE Int. Conf. Robot. Autom. ICRA 2017 (2017)* 1175–1180.
- [42] Y. Gao, L. Wu, D.-M. Yan, L. Nan, Near support-free multi-directional 3D printing via global-optimal decomposition, *Graph. Models* 104 (2019) 101034, <https://doi.org/10.1016/j.gmod.2019.101034>.
- [43] C. Wu, C. Dai, G. Fang, Y.J. Liu, C.C.L. Wang, General support-effective decomposition for multi-directional 3-D printing, *IEEE Trans. Autom. Sci. Eng.* 17 (2) (2020) 599–610, <https://doi.org/10.1109/TASE.2019.2938219>.
- [44] C. Dai, C. Wang, C. Wu, S. Lefebvre, G. Fang, Y.-J. Liu, Support-free volume printing by multi-axis motion, *ACM Trans. Graph.* 37 (2018) 1–14, <https://doi.org/10.1145/3197517.3201342>.
- [45] F. Xie, X. Jing, C. Zhang, S. Chen, D. Bi, Z. Li, D. He, K. Tang, Volume decomposition for multi-axis support-free and gouging-free printing based on ellipsoidal slicing, *Comput. Aided Des.* 143 (2021) 103135, <https://doi.org/10.1016/j.cad.2021.103135>.
- [46] K. Xu, Y. Li, L. Chen, K. Tang, Curved layer based process planning for multi-axis volume printing of freeform parts, *Comput. Aided Des.* 114 (2019) 51–63, <https://doi.org/10.1016/j.cad.2019.05.007>.
- [47] L. Yamin, D. He, X. Wang, K. Tang, Geodesic Distance Field-based Curved Layer Volume Decomposition for Multi-Axis Support-free Printing, *arXiv preprint (2020)* 05938.
- [48] J. Ye, Q. Guo, H. Lu, P. Kyvelou, Y. Zhao, L. Gardner, Y.M. Xie, Topology optimisation of self-supporting structures based on the multi-directional additive manufacturing technique, *Virtual Phys. Prototyp.* 18 (1) (2023) e2271458, <https://doi.org/10.1080/17452759.2023.2271458>.
- [49] H. Lu, L. He, M. Gilbert, F. Gilardi, J. Ye, Design of optimal truss components for fabrication via multi-axis additive manufacturing, *Comput. Methods Appl. Mech. Eng.* 418 (2024) 116464, <https://doi.org/10.1016/j.cma.2023.116464>.
- [50] K. Svanberg, The method of moving asymptotes—a new method for structural optimization 24 (1987) 359–373, <https://doi.org/10.1002/nme.1620240207>.
- [51] Z.H. Zuo, Y.M. Xie, A simple and compact Python code for complex 3D topology optimization, *Adv. Eng. Softw.* 85 (2015) 1–11, <https://doi.org/10.1016/j.advengsoft.2015.02.006>.
- [52] J. Etienne, N. Ray, D. Panozzo, S. Hornus, C.C.L. Wang, J. Martínez, S. McMains, M. Alexa, B. Wyvill, S. Lefebvre, CurviSlicer: slightly curved slicing for 3-axis printers, *Article 81. ACM Trans. Graph.* 38 (2019) <https://doi.org/10.1145/3306346.3323022>.
- [53] Y. Zhou, Q. Lin, J. Hong, N. Yang, Bidirectional evolutionary optimization design of material stiffness for the uniformity of the contact stress, *Eur. J. Mech. A Solids* 89 (2021) 104288, <https://doi.org/10.1016/j.euromechsol.2021.104288>.
- [54] MOSEK Optimizer API for Python. Version 10.0.8. URL: <<https://docs.mosek.com/latest/pythonapi/index.html>>